Applications of DNP and Solid-State NMR for Protein Structure Determination

by

Rebecca Maria Mayrhofer

B.S., Chemical Engineering (2005)

University of Illinois Urbana-Champaign

Submitted to the Department of Chemistry in Partial Fulfillment of the Requirements for the Degree of Master of Science in Chemistry

at the

Massachusetts Institute of Technology

June 2010

Signature of Autho ..... Department of Chemistry

May 19, 2010

Certified by ....

Robert G. Griffin

Professor of Chemistry,

Thesis Supervisor

Accepted by ....

Robert W. Field,

Chairman, Departmental Committee on Graduate Students

Applications of DNP and Solid-State NMR for Protein Structure Determination

by

Rebecca M. Mayrhofer

Submitted to the Department of Chemistry

on May 19, 2010 in Partial Fulfillment of the

Requirements for the Degree of Master of Science

in Chemistry

Abstract

Magic Angle Spinning (MAS) solid state nuclear magnetic resonance (SSNMR) is a developing method for determining the structures and studying the dynamics and functions of biological molecules. This method is particularly important for systems, such as amyloidogenic fibrous proteins, that do not crystallize or dissolve well and are therefore not amendable to X-ray or solution NMR techniques. However, due to inherently low sensitivity, NMR experiments may require weeks to obtain spectra with sufficient signal-to-noise ratio. This issue is further exacerbated for biological systems of interest due to their large size and limited mass availability. The sensitivity can be increased by two orders of magnitude by combining MAS NMR with dynamic nuclear polarization (DNP). The application of SSNMR-DNP to protein structure determination is explored using malonic acid and a model peptide system, WT-$TTR_{105-115}$. A custom built MAS-SSNMR probe is modified for the purpose of MAS-SSNMR DNP experiments.

Thesis Supervisor: Robert G. Griffin

Title: Professor, Department of Chemistry

Director, Francis Bitter Magnet Laboratory

Table of Contents

List of Figures and Tables

Dedication

This thesis is dedicated to my wonderful daughter, Arabella Lorelei Weymouth, born during the 2nd year of my graduate studies as well as my loving husband, Gabriel David Weymouth.

Acknowledgements

I would like to thank my advisor, Professor Robert G. Griffin, for the opportunity to work in his research group and for his guidance and support. I would also like to thank my committee members, Professor Moungi Bawendi and Professor Keith Nelson both for their advice and for the great experience I had as a teaching assistant with them. I truly enjoyed watching them teach and deeply appreciated the respect and trust they had for me as their teaching assistant. I would also like to thank my scholarship agency, A*STAR for funding me throughout my undergraduate and graduate studies.

My work in the laboratory would not have been possible without the immense amount of guidance, assistance and advice I received. Evgeny Markhasin was always there to help me with computer, pulse programming, spectrometer and Autodesk Inventor™ problems. He was also a wonderful confidant – a person I could not only trust but also have fun with. Ta-Chung Ong was also a great friend to me and spent many Saturdays eating salmon at my house. My daughter, Arabella, was especially fond of Evgeny and Ta-Chung, never failing to greet them with smiles and giggles. Without these two, the lab would not have been as much fun. They brightened my day.

I would also like to thank Chris Turner for his advice, help and guidance. Chris taught me all about RNMR and working with spectrometers in the first year of research. Without his help, I would not have gotten as comfortable with pulse programming or running spectrometers. He taught me a lot and I greatly appreciate the many hours he invested, teaching me everything from hardware to theory.

I would also like to thank Thorsten Maly who worked very closely with me on the DNP experiments. I enjoyed working with Thorsten – he helped guide the research in the right direction and was always willing to explain any DNP theory to me. He also listened to my suggestions and respected them. I also enjoyed going to the DNP seminars that Thorsten initiated – his lectures were very informative and helped me learn a lot of the theory of DNP.

Without the help of the Jeffrey Bryant, and Björn, I would not have been able to complete the partially built 211 MHz probe (by Galia, who spent a huge amount of time on it). Björn's guidance and side by side help with the completion of this probe was essential and greatly appreciated!

I would like to thank the remaining lab members for their support and help throughout the years. Matt Eddy for 'helping' me (he did all the work) grow PI3-SH3. Xander for his help with the 211 MHz probe, specifically the sample eject. Loren and Andy for the many hours we spent together, completing coursework. Without their help, it would have been impossible. Especially without Andy's Matlab™ capabilities! And Galia, for her advice on the 211 MHz probe.

Most importantly, I would like to thank my husband, Gabriel, for his wonderful support. He was always there to listen and kept me happy. Not only is he a wonderful husband, but he is also a phenomenal dad!

CHAPTER 1. Introduction to Solid State NMR

Solid state nuclear magnetic resonance is a developing, practical method for determining structure and dynamics in biological molecules. Of the many biophysical techniques in existence, x-ray crystallography and NMR have been the most successful in determining protein structures at atomic resolution. X-ray crystallography and solution state NMR have been used successfully for the elucidation of structural information of soluble globular proteins and their complexes. For non-crystalline, insoluble proteins, magic angle spinning (MAS) solid state NMR (SSNMR) can be employed. Amyloid fibril is a class of proteins that form insoluble protein aggregates. Accumulation of amyloid in organs, amyloidosis, can lead to severe conditions such as Alzheimer's disease, type II diabetes and Parkinson's disease. In the amyloid state, proteins form rope-like fibers. These fibers lack the long-range order necessary for elucidation of atomic level structure via X-ray spectroscopy and are insoluble and thus, cannot be studied via solution NMR. Nevertheless, the fibers are still microscopically ordered and yield high resolution solid state NMR spectra.

Due to the inherently low sensitivity of NMR, experiments may require days or weeks of signal averaging to obtain spectra with sufficient signal-to-noise ratio. Higher sensitivity can be achieved by combining MAS SSNMR with dynamic nuclear polarization (DNP, explained in chapter 2), allowing for elucidation of high resolution structures in a considerable shorter time period.

Although the basics of NMR and DNP is important for understanding the research that follows, only the major concepts of Solid State NMR and DNP (see

chapter 2) that are relevant to this work will be discussed. This will include a brief introduction to NMR as well as basic theory for obtaining distance constraints in proteins with explanations of select pulse sequences. For further reading, see the texts by C.P. Slichter, Malcolm Levitt, John Cavanagh and others.

In basic terms, NMR spectroscopy invokes the excitation of spin polarization with radio frequency (RF) pulses and detection of the signal induction. For each NMR sensitive nuclei, there exists a Larmor frequency (precession frequency), at which the excited spins will precess about the magnetic field, B_o. The magnitude of the Larmor frequency is proportional to the static magnetic field, the constant of proportionality being the gyromagnetic ratio, unique to each NMR sensitive nucleus. In biological systems, the three primary spin ½ nuclei of interest are ^{1}H, ^{13}C and ^{15}N.

The process of determining a high-resolution molecular structure includes the following steps: 1) performing resonance assignments, 2) measurement of distance constraints, and 3) torsion angle constraints. I will focus on the determining the distance constraints, explaining the necessary theory as well as describing specific pulse sequences used for determining ^{13}C-^{13}C distances between degenerate resonances. A brief introduction will be provided for the first and third step.

Nearly complete chemical shift assignment is a prerequisite for the measurements of distances and torsion angles, which are sufficient to refine a structure. The typical experiments performed for backbone and sidechain resonance assignments are homonuclear (^{13}C-^{13}C) and heteronuclear (^{15}N-^{13}C) correlations. Particularly, heteronuclear correlations in their SPECIFIC CP forms are NCA and NCO.

Homonuclear correlations can be used to assign intraresidue cross-peaks while homo/heteronuclear correlations are used for sequential assignments. Further assignments are based on NCACX and NCOCX experiments. These are 2D experiments where the $^{15}N_i$ is one dimension and the $^{13}CA_i$ (as well as its correlated ^{13}C resonances) are in the other dimension. 3D experiments with ^{13}C chemical shifts in two dimensions and ^{15}N chemical shifts in the third dimension can also be performed. The various correlations are illustrated in Figure 1-1 below and the homo- and heteronuclear correlation pulse sequences are shown in Figure 1-2. Once the chemical shifts have been assigned, distance measurements are then used to constrain the structure.

a

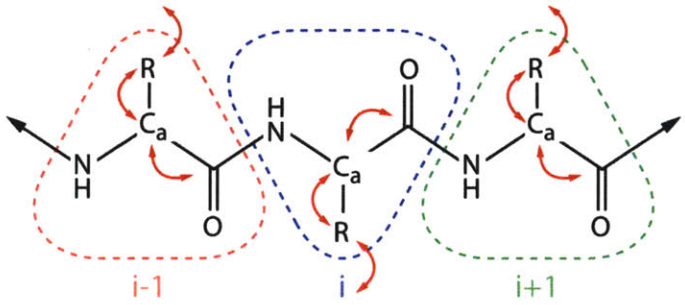

b

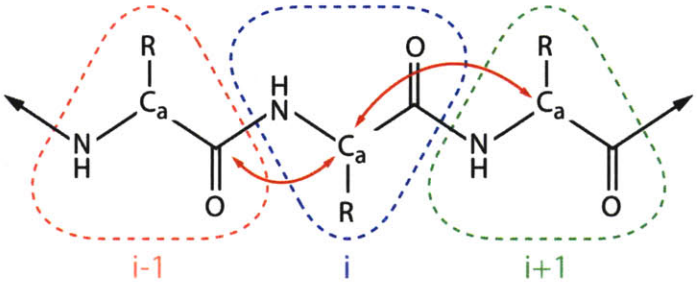

c

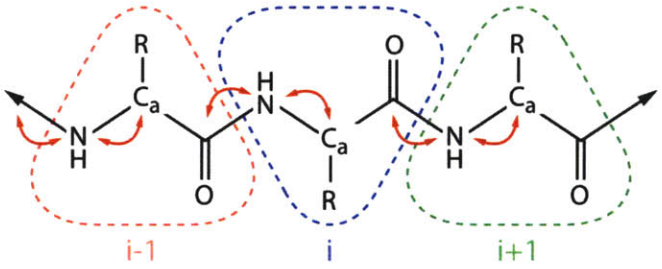

Figure 1-1. Illustration of the various homo- and heteronuclear correlations in a peptide chain

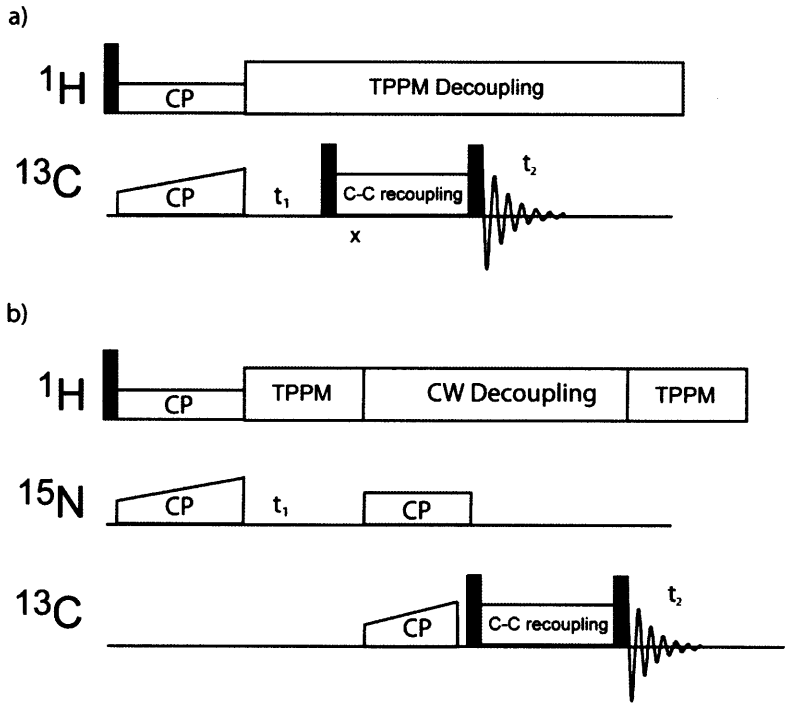

Figure 1-2 a) Generic pulse sequence for a homonuclear correlation experiment used for intraresidue resonance assignment b) Pulse sequence for a heteronuclear correlation experiment used for sequential assignment

In MAS NMR, a sample is rotated at an angle of $\cos^{-1}(\frac{1}{\sqrt{3}})$=54.7° with respect to the static magnetic field (B_o) which effectively averages any second rank tensor interaction such as the chemical shift anisotropy, dipolar coupling and the first order quadrupole coupling that causes line broadening in static samples. [1] Thus, narrow resonance lines similar to those observed in high-resolution solution state NMR are obtained. However, since the homo- and heteronuclear dipolar couplings, which provide information about the structure (such as inter-atomic distances and torsion angles) are also attenuated, it is necessary to reintroduce these couplings by interfering with the MAS averaging mechanism. [1]

Pulse sequences, which reintroduce interactions, are known as recoupling sequences and are comprised of rotor synchronized RF pulse trains that yield a non-zero average dipole coupling. This recoupled interaction is scaled by a factor S, which depends on the specifics of the pulse train. [1] Figure 1-3 below illustrates the dipole recoupling achieved during a MAS experiment in the presence of a RF pulse train. The first Figure (RFDR sequence) shows the modulation of the dipole coupling in the presence of MAS and the absence of a RF pulse train; the average of the dipole coupling is zero. However, when a π pulse is introduced once per rotor period, the dipole coupling reappears, resulting in a non-zero average.

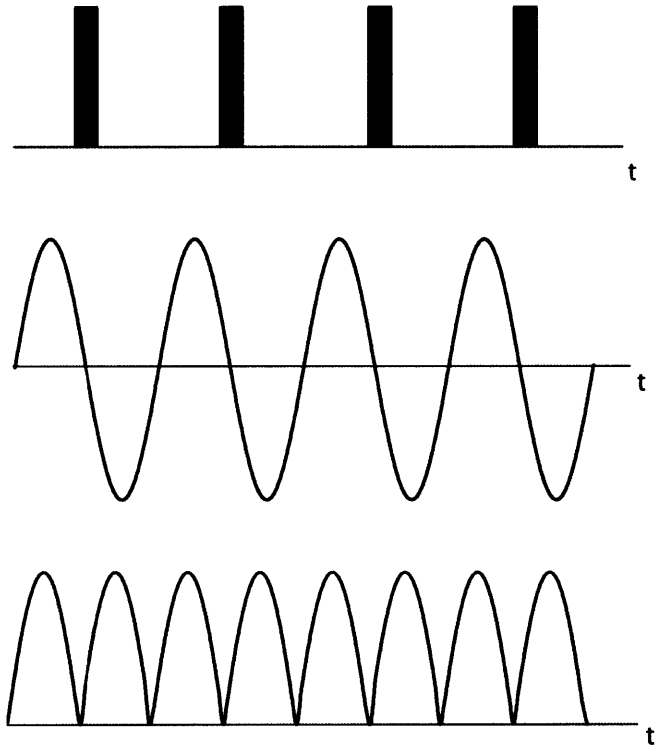

Figure 1-3. Illustration of the dipole coupling and recoupling during MAS a) Rotor synchronized rf π pulses spaced at one per rotor period b) MAS modulates the dipole coupling producing an average of 0 over a rotor period in the absence of rf pulses. c) dipole recoupling in the presence of rotor synchronized π pulses produces a non zero value of $S\omega_D$ where S is the scaling factor. Figure modified from [1]

Examples of pulse sequences used to measure homonuclear distances are DRAWS, DQDRAWS (see below), R^2 and its variants. [2-5] Note that this is just a few examples - there are at least 20 more pulse sequences to measure homonuclear distances. Heteronuclear distances can be measured using pulse sequences such as TEDOR (see below), REDOR and their variants. [6-8] Of particular interest are the pulse sequences, DQDRAWS and TEDOR, described in later sections.

A pulse sequence for measuring homo-nuclear distances is **D**ipolar **R**ecoupling with **A** **W**indowless **S**equence (DRAWS). [2, 9] DRAWS is only good for low spinning frequencies and for large anisotropies. The double quantum DRAWS sequence, shown in Figure 1-4, starts with a cross polarization sequence to transfer the magnetization from the ^1H spins to the ^{13}C spins. Note that the magnetization is in y after the cross-polarization sequence. During cross-polarization, the ^1H spin magnetization is spin locked for a time τ_{cp} during which the RF fields of the ^1H and ^{13}C spins are matched to the Hartmann-Hahn condition, allowing the polarization to be transferred from the ^1H spins to the ^{13}C spins. A strong continuous wave (CW) RF field is applied to the ^1H spins for the remainder of the sequence to decouple the ^1H spins from the ^{13}C spins. The DQDRAWS sequence on the ^{13}C channel consists of two main blocks: the DQC (double quantum coherence) excitation block, followed by the DQC reconversion block. The DQC reconversion block converts the double quantum coherence to observable magnetization (single quantum coherence). As shown in the Figure, the DQC blocks consist of 8 2π pulses and 2 $\pi/2$ pulses. The 2π pulses suppress the chemical shifts and the phase alteration of these pulses helps to compensate for RF in homogeneity. The $\pi/2$ pulses in the R block prevent the averaging of the dipolar interaction. The

entire sequence is supercycled to give the sequence $R\overline{RRR}$. This is because a single cycle (one R block) of DRAWS does not completely suppress the chemical shift Hamiltonian [9].

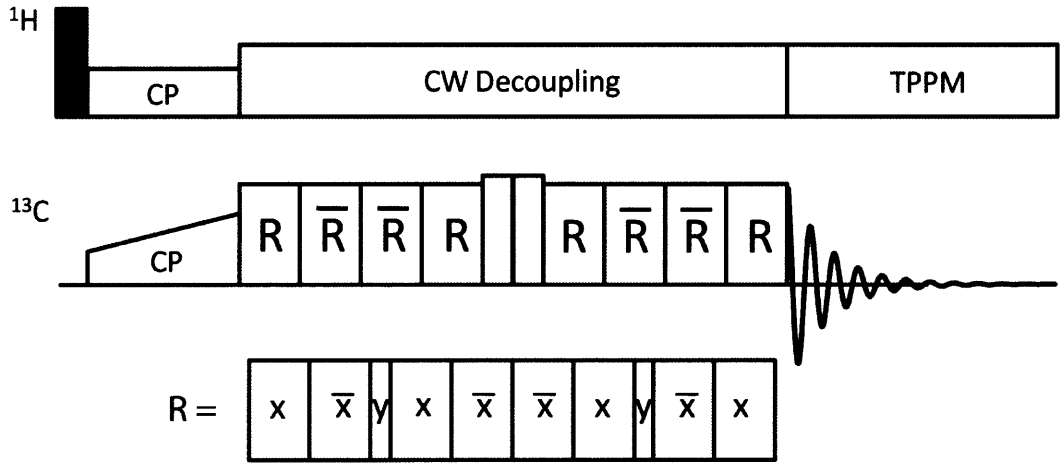

Figure 1-4. Pulse Sequence for DQDRAWS on the ^{13}C observe channel. The white block is the excitation block and the shaded block is the reconversion block. Note that the magnetization starts in y for the DRAWS sequence. The length of the R block, τ_r, is one rotor period. For an MAS frequency of 5.882 kHz, this corresponds to a 2π pulse of duration 20 μs. [9]

The DRAWS sequence can be described using average Hamiltonian theory. [9] The full propagator for the time dependent Hamiltonian is

$$U(t) = T\exp\left(-i\int_0^1 dt' H(t')\right) \tag{1}$$

where T is the Dyson time ordering operator. Using the Magnus expansion, the time independent effective Hamiltonian, is

$$U(t) = \exp\{-i\overline{H}T\} = \exp\left\{-i\left[\overline{H}^{(0)} + \overline{H}^{(1)} + \overline{H}^{(2)} + \cdots\right]\right\} \tag{2}$$

where the 0th order the 1st order Hamiltonian are given by

$$\overline{H}^{(0)} = \frac{1}{t}\int_0^1 dt' H(t')$$

$$\overline{H}^{(0)} = \frac{-i}{2t}\int_0^1 dt''\left[H(t''), H(t')\right]$$

The higher terms in the expansion arise because the Hamiltonian does not commute with itself at different times. In the DRAWS sequence (one of the blocks of the $R\overline{R}\overline{R}R$ sequence), the r.f. is continually on; a toggling frame transformation is required to obtain finite pulse widths. In this transformation, the chemical shift and dipolar Hamiltonian (internal) becomes time dependent and the r.f. term is eliminated (as they are transformed into the interaction frame of the r.f.). The time dependence of the internal Hamiltonian in the toggling frame is given by

$$H_{tog}^{(\mathrm{int})} = U_{r.f.}^{-1} H^{\mathrm{int}} U_{r.f.} \tag{3}$$

where the propagator is given by

$$U_{r.f.} = T\exp\left\{-i\int_0^1 dt' H_{r.f.}\right\} \tag{4}$$

The DRAWS zeroth order average Hamiltonian for a pair of dipolar-coupled spins on resonance and spinning at the magic angle has the form

$$H_D^{(0)} = \frac{d}{17\pi}\left[c_{xx-yy}\left(I_x S_x - I_y S_y\right) + c_{zz}\left(3I_z S_z - I\cdot S\right)\right] \tag{5}$$

where $d = \frac{\mathrm{h}\gamma^2}{r^3}$ is the static dipolar coupling in $\mathrm{rad}^{-1}\mathrm{s}$. The coefficients, c_{xx}, c_{yy}, and c_{zz} are functions of the Euler angles orienting the principle axis of the dipolar tensor in the frame of the rotor. To zeroth order, the DRAWS supercycle completely suppresses the

chemical shift terms. The DRAWS sequence recouples the dipolar interaction, such that in the zeroth order average Hamiltonian, the dipolar coupling term is reintroduced.

As shown in Figure 1-4, each DRAWS sequence (the R element) has an overall tipping angle of 17π. To find the r.f. field strength required on the carbon channel, the following relation can be used

$$\frac{\theta_r}{\omega_r} = \frac{\theta_{r.f.}^S}{\omega_{r.f.}^S} \tag{6}$$

where θ_r is the angle or rotation, ω_r is the MAS frequency, $\theta_{r.f.}$ is the tipping angle and $\omega_{r.f.}$ is the r.f. field strength. Since θ_r is 2π and $\theta_{r.f.}$ is 17π,

$$\frac{2\pi}{\omega_r} = \frac{17\pi}{\omega_{r.f.}^S}$$

$$\omega_{r.f.}^S = 8.5x\omega_r$$

Figure 1-5 below shows a typical build up curve obtained using DQDRAWS for ammonium succinate. Using NMR simulation software, such as SPINEVOLUTION, the experimental curve can be simulated to determine the internuclear distance. [10]

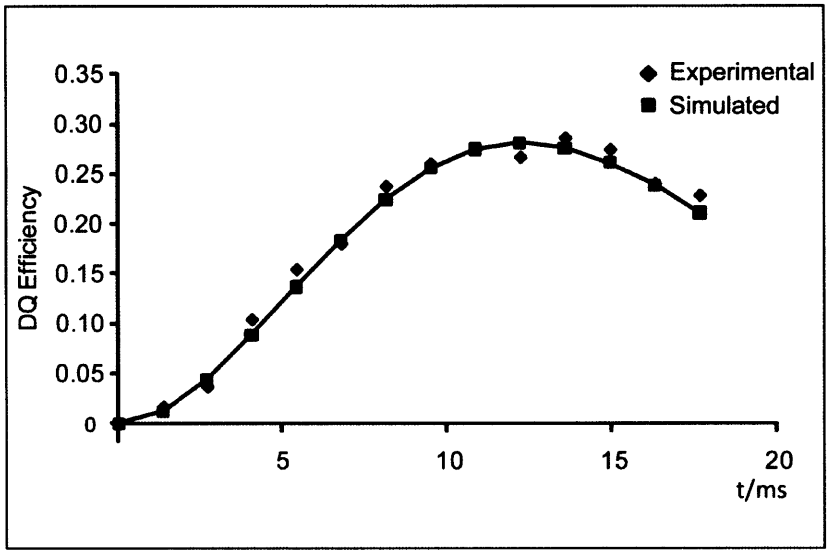

Figure 1-5. Double quantum buildup curve for 1,4-^{13}C-succinate using 100 kHz proton and simulation using SPINEVOLUTION. Data were collected on a 360 MHz spectrometer using 4 mm rotors and $\omega_r/2\pi$ = 5.882 kHz.

Currently, these experiments are tedious as each data point requires a significant number of acquisitions to obtain sufficient signal to noise ratio. Combining this experiment with DNP would allow for a much shorter data acquisition time, resulting in faster elucidation of structural information. The model system, WT-$TTR_{105-115}$ as well as its mutant form, L111M, can be used to study DNP- DQDRAWS.

Transferred **E**cho **DO**uble **R**esonance (TEDOR) is a heteronuclear recoupling pulse sequence. This sequence can be used for simultaneous peak assignment and multiple distance measurements. [6] It is particularly useful as it provides the capability of measuring multiple dipolar couplings of heteronuclear I-S pairs. The modified pulse sequence is provided in Figure 1-6 below. [7]

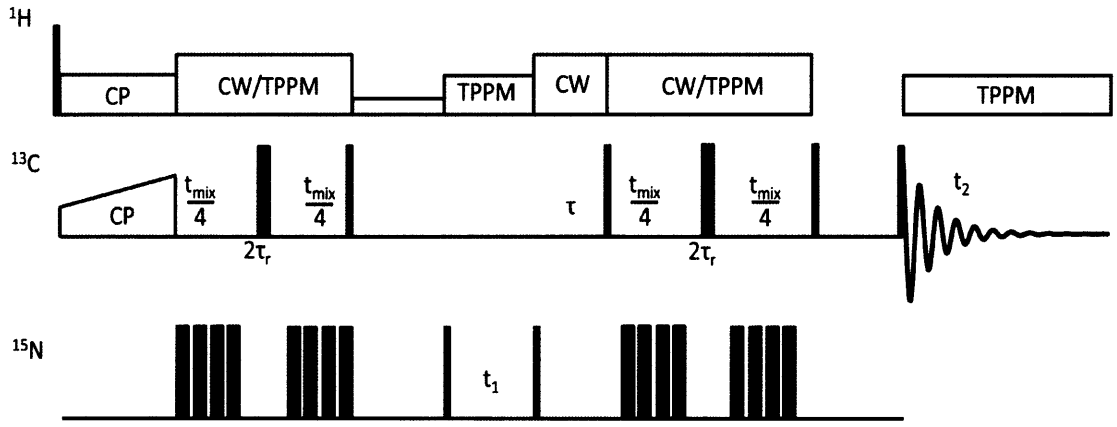

Figure 1-6. z-filtered TEDOR pulse sequence. Narrow and wide rectangles represent π/2 and π pulses, respectively. A weak proton rf field is applied during the z filter to facilitate the rapid dephasing of the ^{13}C coherences via contact with the proton bath. [7]

In the TEDOR pulse sequence, initial ^{13}C magnetization is transferred to ^{15}N for frequency labeling and then transferred back to ^{13}C for detection. The mixing periods are REDOR mixing periods, obtained from the REDOR pulse sequence. ^{13}C-^{15}N distances can be extracted using simple build up curves (as described in the previous section) of the cross peak intensity versus the mixing time. [11] These build up curves are then simulated with SPINEVOLUTION.

The coherence transfer pathway, with initial magnetization, I_x (created via cross polarization), after the REDOR mixing period is

$$I_x \rightarrow 2I_y S_z \sin\left(\frac{\omega t_{mix}}{2}\right)$$

This reintroduces the I-S dipolar coupling and generates I-spin coherence (I_y), which is anti-phase to the S spin coherence (S_z). Following the REDOR mixing period, a π/2 pulse is applied to the I and S spins in the x-direction. As the respective pulses only affect the I or S spin, the propagator can be applied sequentially,

$$U = e^{iI/S_{x/y/z}\phi}$$

where ϕ is the pulse duration

$$e^{iI_x\frac{\pi}{2}} 2I_yS_z \sin\left(\frac{\omega t_{mix}}{2}\right) e^{-iI_x\frac{\pi}{2}}$$

$$2I_yS_z \sin\left(\frac{\omega t_{mix}}{2}\right)\cancel{\cos\left(\frac{\pi}{2}\right)} + 2I_zS_z \sin\left(\frac{\omega t_{mix}}{2}\right)\sin\left(\frac{\pi}{2}\right)$$

Applying the propagator for the S spin for a π/2 pulse,

$$e^{iS_x\frac{\pi}{2}} 2I_zS_z \sin\left(\frac{\omega t_{mix}}{2}\right)\sin\left(\frac{\pi}{2}\right) e^{-iS_x\frac{\pi}{2}}$$

$$2I_zS_z \sin\left(\frac{\omega t_{mix}}{2}\right)\cancel{\cos\left(\frac{\pi}{2}\right)} - 2I_zS_y \sin\left(\frac{\omega t_{mix}}{2}\right)\sin\left(\frac{\pi}{2}\right)$$

After t_1 evolution,

$$-2I_zS_y \sin\left(\frac{\omega t_{mix}}{2}\right)\sin\left(\frac{\pi}{2}\right) \rightarrow -2I_zS_y \sin\left(\frac{\omega t_{mix}}{2}\right) e^{i\Omega_s t_1}$$

Following t_1 evolution, π/2 pulses are applied to the I and S spin which transfer the coherence back to the I spin. Applying the π/2 pulse to the I spin first (the cosine term is zero as shown above),

$$e^{iI_{-x}\frac{\pi}{2}} - 2I_zS_y \sin\left(\frac{\omega t_{mix}}{2}\right) e^{i\Omega_s t_1}\ e^{-iI_{-x}\frac{\pi}{2}} \rightarrow 2I_yS_y \sin\left(\frac{\omega t_{mix}}{2}\right) e^{i\Omega_s t_1}$$

Applying the π/2 pulse to the S spin (again, the cosine term is zero)

$$e^{iS_x\frac{\pi}{2}}2I_yS_y\sin\left(\frac{\omega t_{mix}}{2}\right)e^{i\Omega_s t_1}\ e^{-iS_x\frac{\pi}{2}} \rightarrow 2I_yS_z\sin\left(\frac{\omega t_{mix}}{2}\right)e^{i\Omega_s t_1}$$

A second REDOR mixing period is applied during which the anti-phase coherence is converted back to observable I-spin magnetization

$$2I_yS_z\sin\left(\frac{\omega t_{mix}}{2}\right)e^{i\Omega_S t_1} \rightarrow 2I_x\sin^2\left(\frac{\omega t_{mix}}{2}\right)e^{i\Omega_S t_1}$$

The resulting magnetization evolves under t_2 during acquisition resulting in frequency labeling with the I chemical shift, Ω_I.

$$2I_x\sin^2\left(\frac{\omega t_{mix}}{2}\right)e^{i\Omega_S t_1} \rightarrow 2I_x\sin^2\left(\frac{\omega t_{mix}}{2}\right)e^{i\Omega_S t_1}e^{i\Omega_I t_2}$$

This results in a 2D spectrum with cross-peaks at frequencies (Ω_I, Ω_S). Proton coupling is removed via decoupling during the pulse sequence and acquisition. TEDOR can also be combined with DNP to give shorter data acquisition times, resulting in fast elucidation of structural information.

The third step in high-resolution structure determination is determining torsion angle constraints. They yield precise conformational information, such as the secondary structure of polypeptides and other biomolecules. Torsion angles are determined using dipolar recoupling techniques that correlate the orientation of two tensors such as two dipole tensors or dipole and CSA tensors [12].

There are four torsion angles in a peptide. These are ϕ, ψ, ω, and χ, which are depicted in Figure 1-7.

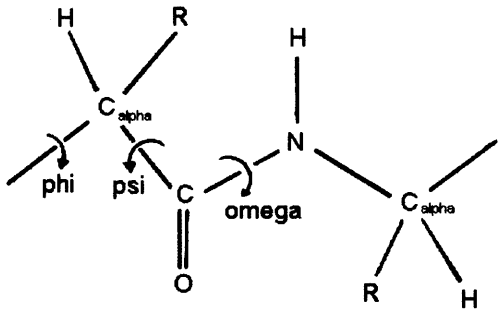

Figure 1-7. Definition of the torsion angles. The orientation of the two peptide planes are described by the torsion angles, ϕ and ψ which are around the N-Cα and Cα-C bond. The dihedral angle, χ, is the side chain angle. The angle, ω, is around the N-C' bond.

References

1. Griffin, R. G., Dipolar recoupling in MAS spectra of biological solids. *Nature Structural Biology* **1998,** *5*, 508-512.
2. Gregory, D. M.; Mitchell, D. J.; Stringer, J. A.; Kiihne, S.; Shiels, J. C.; Callahan, J.; Mehta, M. A.; Drobny, G. P., Windowless dipolar recoupling--The detection of weak dipolar couplings between spin-1/2 nucleic with large chemical-shift anisotropies. *Chem. Phys. Lett.* **1995,** *246*, 654.
3. Gregory, D. M.; Mehta, M. A.; Shiels, J. C.; Drobny, G. P., Determination of local structure in solid nucleic acids using double quantum nuclear magnetic resonance spectroscopy. *J. Chem. Phys.* **1997,** *107* (1), 28-42.
4. Raleigh, D. P.; Levitt, M. H.; Griffin, R. G., Rotational Resonance in solid state NMR. *Chem.Phys.Letters* **1988,** *146*, 71-76.
5. Lakshmi, K. V.; Auger, M.; Raap, J.; Lugtenburg, J.; Griffin, R. G.; Herzfeld, J., Internuclear Distance Measurement in a Reaction Intermediate - Solid-State C-13 Nmr Rotational Resonance Determination of the Schiff-Base Configuration in the M-Photointermediate of Bacteriorhodopsin. *J Am Chem Soc* **1993,** *115* (18), 8515-8516.
6. Hing, A. W.; Vega, S.; Schaefer, J., Transfer Echo Double Resonance NMR. *J. Magn. Reson.* **1992,** *96*, , 205-209.
7. Jaroniec, C. P.; Filip, C.; Griffin, R. G., 3D TEDOR NMR experiments for the simultaneous measurement of multiple carbon-nitrogen distances in uniformly C-13, N-15- labeled solids. *J Am Chem Soc* **2002,** *124* (36), 10728-10742.
8. Gullion, T.; Schaefer, J., Rotational-Echo Double-Resonance NMR. *J. Magn. Reson.* **1989,** *81*, 196-200.
9. Mehta, M. A.; Gregory, D. M.; Kiihne, S.; Mitchell, D. J.; Hatcher, M. E.; Shiels, J. C.; Drobny, G. P., Distance measurements in nucliec acids using windowless dipolar recoupling solid state NMR. *Solid State Nucl. Mag. Reson.* **1996,** *7* (3), 211-228.
10. Spector, T., Ribonucleotide Reductases Encoded by Herpes Viruses: Inhibitors and Chemotherapeutic Considerations. In *Inhibitors of Ribonucleoside Diphosphate Reductase Activity*, Cory, J. G.; Cory, A. H., Eds. Pergamon Press: New York, 1989; pp 235-243.
11. Jaroniec, C. P.; Lansing, J. C.; Tounge, B. A.; Belenky, M.; Herzfeld, J.; Griffin, R. G., Internuclear distance measurements in uniformly C-13, N-15 labeled peptides and proteins. *Biophysical Journal* **2002,** *82* (1), 2288.
12. Feng, X.; Lee, Y. K.; Sandstrom, D.; Eden, M.; Maisel, H.; Sebald, A.; Levitt, M. H., Direct determination of a molecular torsional angle by solid-state NMR. *Chem. Phys. Lett.* **1996,** *257*, 314-320.

CHAPTER 2. Introduction to Dynamic Nuclear Polarization

DNP was first realized using the concept of the electron-nuclear Overhauser effect (OE), theoretically predicted by Albert Overhauser in 1953 and observed experimentally by Carver and Slichter in Li metal in 1953. [5-6] Since its discovery, DNP has gained wide recognition for its potential and has been studied extensively. [1] Current applications of DNP include small-molecule spectroscopy, and MAS studies of biological systems such as virus capsids, membrane proteins, lipids and amyloidogenic proteins. [2-3] The application of DNP to protein structure determination would dramatically decrease the duration of an experiment due to the significant signal enhancements made available from the technique.

In DNP, irradiation of the EPR spectrum with microwaves transfers the larger electron polarization to the nuclear spin system via one of the mechanisms described below. The theoretical enhancement is $\gamma_e/\gamma_n \sim 660$. Figure 2-1 shows the signal enhancement achieved by DNP on a sample of proline.

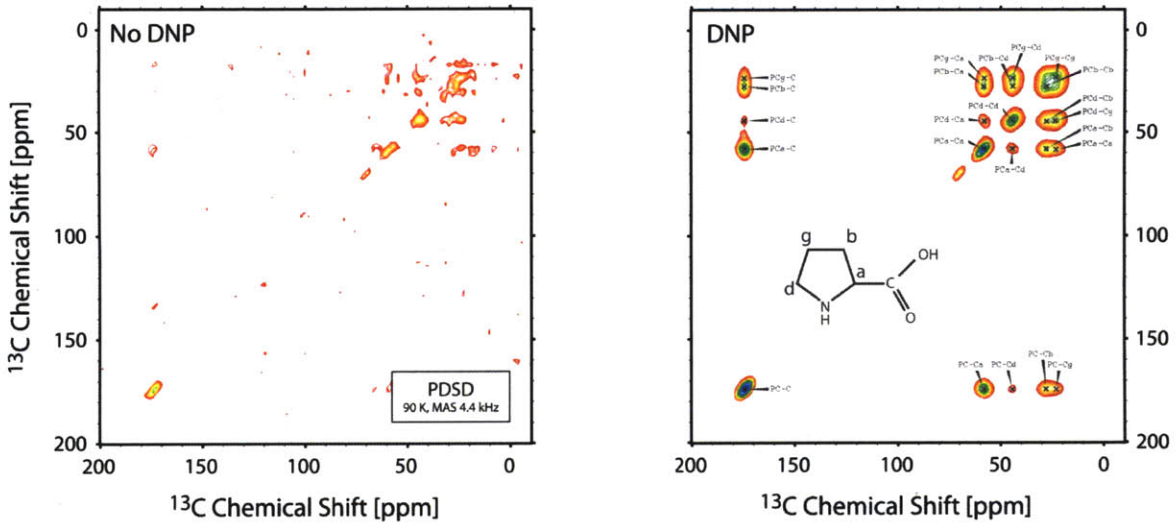

Figure 2-1. 2-D PDSD spectrum of Proline and a 2D-DNP PDSD spectrum of Proline. Note the enhancement in the signal to noise ratio for the spectrum taken with DNP. Spectra were taken at 90 K with a MAS frequency of 4.4 kHz. Figure courtesy of T. Maly.

Four of the mechanisms that mediate DNP are: 1) the Overhauser effect 2) the solid effect (SE), 3) the thermal mixing effect (TM), and 4) the cross effect (CE). [1, 4] Unlike the other mechanisms of DNP, the Overhauser Effect relies on time dependent electron-nuclear and electron-electron interactions, which simultaneously flips an electron and a nuclear spin. [1] In solution, these relaxation processes are from the time dependent dipolar and scalar interactions between the electrons and the nuclei. In insulating solids, the presence of mobile electrons such as those found in metals, are not available. Hence, this mechanism is not relevant in the DNP experiments considered here.

The latter three mechanisms, SE, TM and CE, are distinguished by comparing the EPR spectrum breadth, Δ, to the size of the nuclear Larmor frequency, ω_n. In particular, the SE dominates when $\Delta < \omega_n$, whereas the CE and TM mechanisms are important when $\Delta > \omega_n$. The CE and TM are further differentiated by whether or not the

EPR spectrum is inhomogeneously broadened by the g-anisotropy and electron cross relaxation or by homogeneous broadening from the electron-electron dipolar coupling, respectively.

The solid effect is the simplest of the DNP mechanisms and involves the simultaneous spin flips of an electron and a coupled nucleus. [7] The solid effect is useful as a pedagogical tool to understand DNP as it is a simple mechanism. The Figure below illustrates the solid effect.

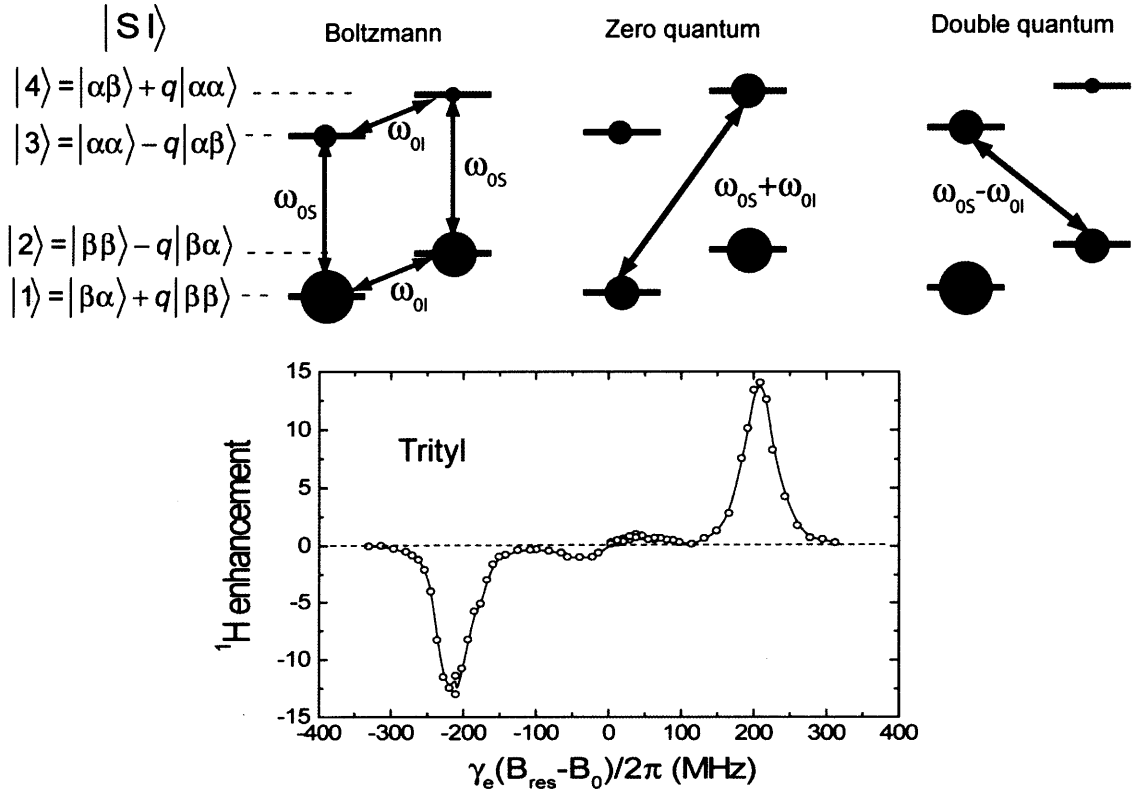

Figure 2-2. Illustration of the solid effect. SE dominates when $\Delta < \omega_n$. Zero quantum transition results in negative enhancement and double quantum transitions in positive enhancement. The mixing of the wavefunctions can be determined using first order perturbation theory. The admixture coefficient is q. The radical, trityl can be used to achieve the solid effect.

It is governed by the following time independent Hamiltonian

$$H_O^{SI} = \omega_{OS} S_Z - \omega_{OI} I_Z + A S_Z I_Z + B S_Z I_X \quad (1)$$

where $\omega_{OS}S_z$ and $\omega_{OI}I_z$ are the electron and nuclear Zeeman terms in the laboratory frame, respectively and A and B are the secular and non-secular parts of the hyperfine coupling.

For the solid effect, a dipolar coupling between the electron and the nucleus is required. The Hamiltonian, which governs this interaction, is

$$H_{HF}^{aniso} = \frac{\gamma_I \gamma_m \hbar}{r^2}[A + B + C + D + E + F] \quad (2)$$

$$A = (1 - 3cos^2\theta) S_z I_z$$

$$B = -\frac{1}{4}(1 - 3cos^2\theta)(S^+ I^- + S^- I^+)$$

$$C = -\frac{3}{2} sin\theta cos\theta e^{-i\varphi} (S_z I^+ + S^+ I_z)$$

$$D = -\frac{3}{2} sin\theta cos\theta e^{i\varphi} (S_z I^- + S^- I_z)$$

$$E = -\frac{3}{4} sin^2\theta e^{-2i\varphi} S^+ I^+$$

$$F = -\frac{3}{4} sin^2\theta e^{2i\varphi} S^- I^-$$

The terms A and B commute with the Zeeman interaction and are referred to as the secular terms; one spin-flip terms are described by C and D and double quantum two spin flip terms are described by E and F. The off-diagonal terms, C, D, mix the electron

and nuclear eigenstates (resulting in an admixture). This enables a microwave field (in the case of DNP) to induce transitions which are weakly allowed due to the first order perturbation of the non-secular dipolar interaction. The admixture coefficient is given by [1]:

$$q = \frac{3}{2}\frac{\gamma_I \gamma_S \mathrm{h}}{2r^3 \omega_n} \sin\theta\cos\theta e^{-i\varphi} \tag{3}$$

It is also interesting to note that as the nuclear Larmor frequency, ω_n, increases (larger magnetic fields), q becomes smaller giving rise to a smaller DNP effect.

Polarization is generated by irradiating the electrons at $\omega_e \pm \omega_n$ which generates negative zero quantum and positive double quantum enhancements, respectively. To determine how the enhancement of the solid effect scales with the B_o field, the Hamiltonian from equation 2 can be diagonalized by the unitary transformation

$$U = \exp[-i(\eta_\alpha S^\alpha I_y + \eta_\beta S^\beta I_y)] \tag{4}$$

where

$$\eta_\alpha = \tan^{-1}\theta\left(\frac{-B}{A + 2\omega_1}\right)$$

$$\eta_\beta = \tan^{-1}\theta\left(\frac{-B}{A - 2\omega_1}\right)$$

$$S^{\alpha,\beta} = \frac{1}{2}(1E \pm S_Z)$$

to give the Hamiltonian

$$H = \omega_{OS} S_Z + \omega_I I_Z + A S_Z I_Z + \omega_I \cos(\eta)\, S_x + 2\omega_I \sin(\eta)\, S_y I_y \quad (5)$$

where

$$\eta = \frac{\eta_\alpha - \eta_\beta}{2}$$

The last two terms arise from the microwave excitation and are responsible for the allowed and forbidden transition, respectively. The microwave Hamiltonian can be re-written as

$$H = \omega_I \cos(\eta)\, S_x + \tfrac{1}{2}\omega_I \sin(\eta)\,[S^+ I^- + S^- I^+] - \tfrac{1}{2}\omega_I \sin(\eta)\,[S^+ I^+ + S^- I^-] \quad (6)$$

Since η is very small, sin(η) ~ η, the forbidden transition probability is proportional to η^2. As η is small,

$$\eta_\alpha : \left(\frac{-B}{A + 2\omega_I}\right)$$

$$\eta_\beta : \left(\frac{-B}{A - 2\omega_I}\right)$$

Thus,

$$\eta = \frac{\eta_\alpha - \eta_\beta}{2} = -B\left(\frac{1}{A + 2\omega_I} - \frac{1}{A - 2\omega_I}\right)$$

$$= -B\left(\frac{4\omega_I}{A^2 - 4\omega_I^2}\right)$$

Since A is the secular term, ω_I dominates and this can be simplified to

$$\eta = B\left(\frac{1}{\omega_I}\right)$$

Thus, the forbidden transition probability (which is proportional to η^2 as mentioned previously) is proportional to ω_I^{-2}. As ω_I is also proportional to the B_o field, the enhancement for the solid effect scales as B_o^{-2}.

Thermal mixing was first described in the 1970's by Goldman, et al, followed by Wenckebach et al and Duijvestijn et al. [12-14] Thermal mixing is a multi spin process operative when the breadth of the EPR exceeds the nuclear Larmor frequency. [8] When these multi spin criteria are met, the nuclear and electron Zeeman reservoirs are indirectly coupled by their mutual interaction with the reservoir corresponding to the secular part of the dipolar interaction Hamiltonian. Cooling of the latter reservoir can then result in increased nuclear polarization.

For thermal mixing to take place, the relation, $\Delta \sim \delta > \omega_{OI}$, where Δ is the inhomogenous breadth, δ the homogenous linewidth and ω_{OI} nuclear Larmor frequency must be met and this enables the following matching condition to be obtained:

$$\omega_{OS2} - \omega_{OS1} = \omega_I \tag{7}$$

where ω_{OS1} and ω_{OS2} are the EPR frequencies of two dipolar coupled electrons, respectively. To satisfy the condition, $\delta > \omega_{OI}$ at low magnetic fields, it is necessary that the concentration of the polarizing agent be high which affects the resolution of an SSNMR experiment. At high fields, however, the inhomogeneous breadth is much greater than the homogenous linewidth and so we do not really observe thermal mixing.

The cross effect involves a three-spin process, involving the interaction between two unpaired electrons and a single nuclear spin. [4] As shown in Figure 2-2, this results in eight energy levels. Microwave irradiation can drive polarization transfer by irradiating the transitions shown in Figure 2-2. The states, |2> and |7>, are coupled through electron-electron and electron-nucleus interactions, allowing this transition to take place. Note that when the matching condition from equation 5 is satisfied, then the DNP efficiency improves as the energy levels, |2> and |7>, become degenerate.

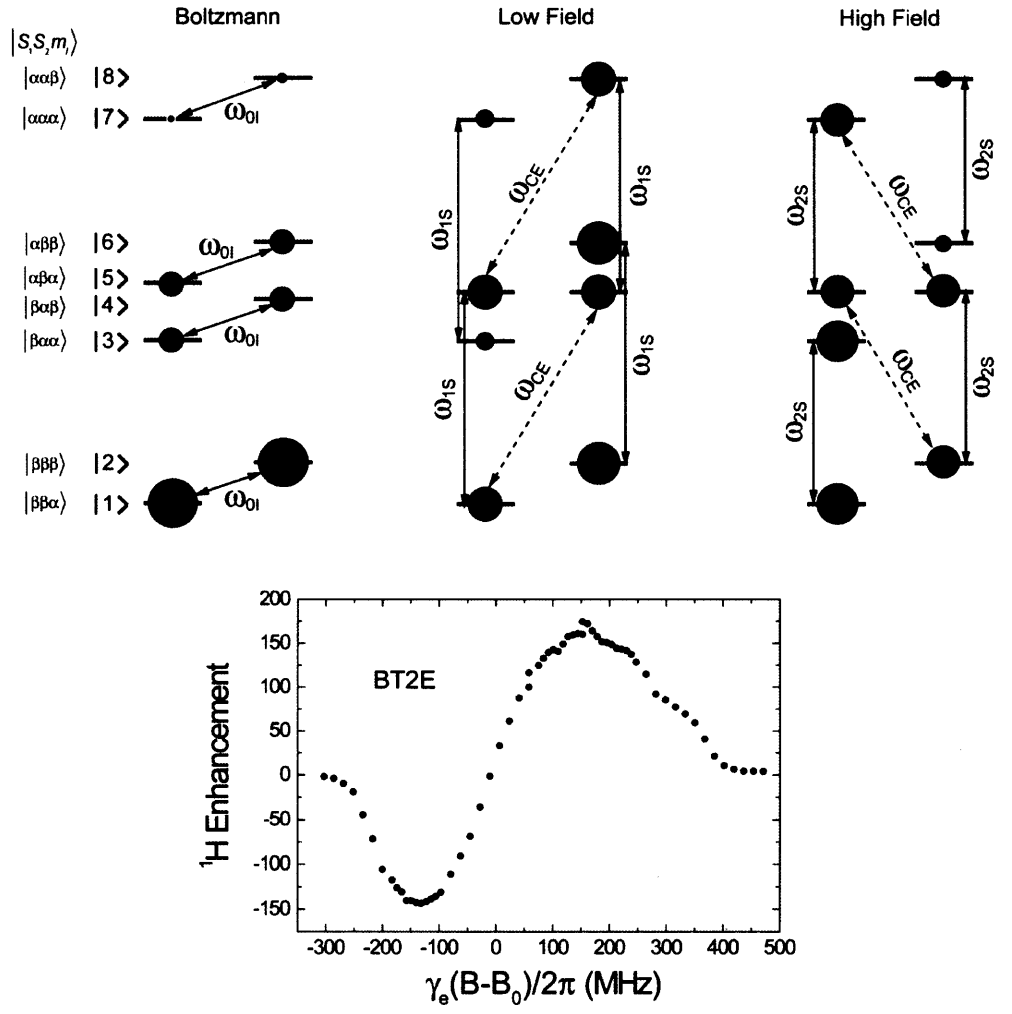

Figure 2-3. Energy levels associated with the cross effect (CE). There are 8 energy levels associated with the CE as this mechanism involves paired electrons. The probability of electron-nuclear transitions can be large in the CE (or TM), especially when there is degeneracy between the states with alternating nuclear spin quantum numbers. Cross effect is shown for both low and high field. The radical, BT2E can be used to achieve enhancement via the CE.

Recently, the biradical, TOTAPOL, consisting of two TEMPO moieties tethered by a three-carbon chain, was introduced and substantial enhancement in nuclear spin polarization has been observed. In general, biradicals yield larger DNP enhancements over shorter polarizing times and at lower concentrations (~10 mM). Other biradicals that have been studied include BTnE, BTurea, and BTOXA. Although B2TE has demonstrated superior DNP performance, it is not soluble in glycerol/water. Thus, the biradical of choice is TOTAPOL which provides enhancements very close to what BT2E has shown. The Figure below illustrates the some of the radicals used in DNP.

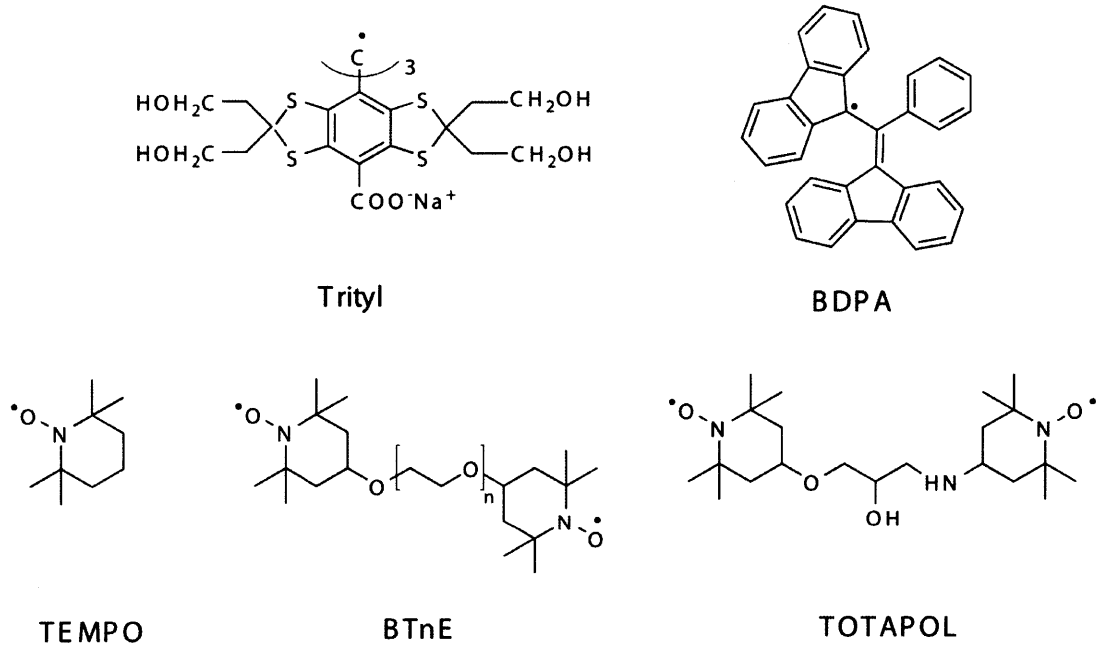

Figure 2-4. Illustration of the radicals used in DNP.

The electrons involved in the cross-effect do not necessarily need to come from the same radical; Hu et. al. demonstrated that using a mixture of two radicals, TEMPO and trityl (or BDPA and trityl) resulted in greater enhancement than by using solely TEMPO. [9] The ideal polarizing agent for CE experiments consists of two radicals with isotropic g-values separated by $|\omega_{e1} - \omega_{e2}| = \omega_n$ which is closely met by the mixture of two radicals.

Instrumentation

Performing modern solid-state NMR experiments with high frequency microwave irradiation for DNP requires several pieces of instrumentation. A source of microwaves at the electron Larmor frequency, a means to deliver the microwaves to the sample, and a cryogenic MAS probe allowing mechanical rotation of the sample rotor as well as application of strong B_1 fields at the nuclear Larmor frequency are required. [4, 10-11] Below are photographs of a rotor, gyrotron, magnet, and transmission line.

Rotor

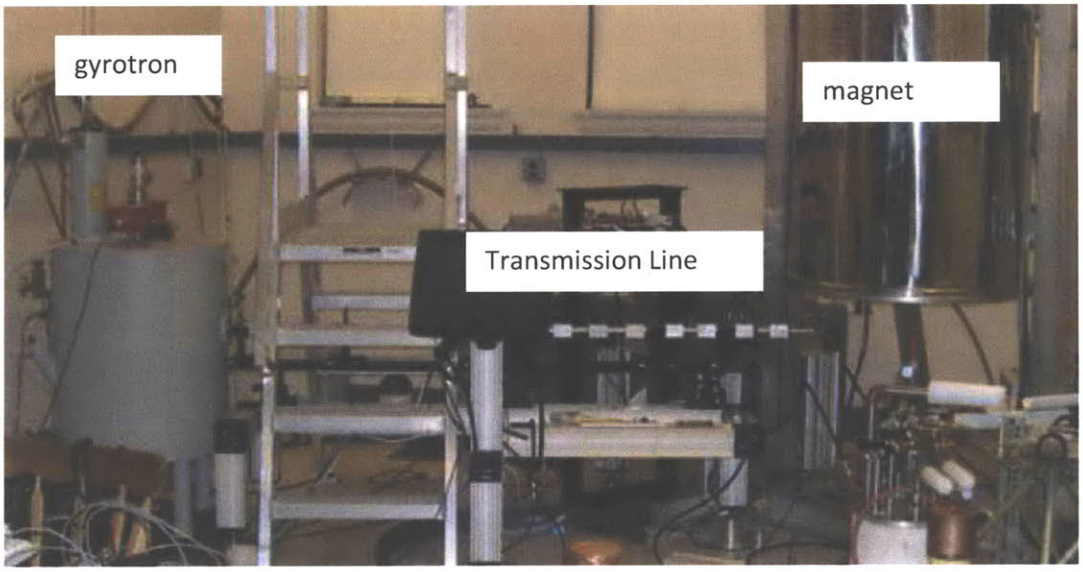

Figure 2-5. Photographs of rotor, gyrotron, transmission line and magnet

MAS NMR- DNP experiments were conducted on a 211 MHz spectrometer connected to a 140 GHz gyrotron.

References

1. Maly, T.; Debelouchina, G. T.; Bajaj, V. S.; Hu, K.-N.; Joo, C.-G.; Mak-Jurkauskas, M. L.; Sirigiri, J. R.; Wel, P. C. A. v. d.; Herzfeld, J.; Temkin, R. J.; R. G. Griffin, Dynamic Nuclear Polarization at High Magnetic Fields. *J. Chem Physics* **2008,** *128*, 052211.
2. Bajaj, V. S.; Farrar, C. T.; Hornstein, M. K.; Mastovsky, I.; Vieregg, J.; Bryant, J.; Elena, B.; Kreischer, K. E.; Temkin, R. J.; Griffin, R. G., Dynamic nuclear polarization at 9T using a novel 250 GHz gyrotron microwave source. *J. Mag. Res.* **2003,** *160*, 85-90.
3. Griffin, R. G., High frequency dynamic nuclear polarization. *Abstracts of Papers of the American Chemical Society* **2005,** *229*, U721-U721.
4. Barnes, A. B.; Paëpe, G. D.; Wel, P. C. A. v. d.; Hu, K.-N.; Joo, C.-G.; Bajaj, V. S.; Mak-Jurkauskas, M. L.; Sirigiri, J. R.; Herzfeld, J.; Temkin, R. J.; Griffin, R. G., High Field Dynamic Nuclear Polarization for Solid and Solution Biological NMR. *Applied Magnetic Resonance* **2008**, (in press).
5. Overhauser, A. W., Polarization of Nuclei in Metals. *Phys. Rev.* **1953,** *92*, 411-415.
6. Carver, T. R.; Slichter, C. P., Polarization of Nuclear Spins in metals. *Physical Review* **1953,** *92*, 212-213.
7. Abragam, A.; Proctor, W. G., Solid Effect. *C.R. Acad. of Sci.* **1959,** *246*, 2253.
8. Borghini, M.; Boer, W. D.; Morimoto, K., Nuclear Dynamic Polarization by Resolved Solid-Effect and Thermal Mixing
with an Electron Spin-Spin Interaction Reservoir. *Physics Letters* **1974,** *48A* (4), 244-246.
9. Hu, K.-N.; Bajaj, V. S.; Rosay, M. M.; Griffin, R. G., High Frequency Dynamic Nuclear Polarization Using Mixtures of TEMPO and Trityl Radicals. *J. Chem. Phys.* **2007,** *126*, 044512.
10. Farrar, C. T.; Hall, D. A.; Gerfen, G. J.; Rosay, M.; Ardenkjaer-Larsen, J. H.; Griffin, R. G., High-frequency dynamic nuclear polarization in the nuclear rotating frame. *J Magn Reson* **2000,** *144* (1), 134-141.
11. Farrar, C. T.; Hall, D. A.; Gerfen, G. J.; Inati, S. J.; Griffin, R. G., Mechanism of dynamic nuclear polarization in high magnetic fields. *J Chem Phys* **2001,** *114* (11), 4922-4933.
12. Goldman, M. Thermal Mixing between Spin Systems in Solids. *Phys. Rev.* **1965,** *138* (6A), A1668-A1674.
13. Wenckebach, W. Th.; Swanenburg, T.J.B; Poulis, N.J. Thermodynamics of spin systems in paramagnetic crystals. *Phys. Rept.* **1974,** *14* (5) 181-255
14. Duijvestijn, M.J.; Wind, R.A.; Smidt, J. A quantitative investigation of the dynamic nuclear polarization effect by fixed paramagnetic centra of abudnant and rare spins in solids at room temperature. *Physica B&C.* **1983** *138* (1-2) 147-170.

CHAPTER 3. Introduction to Amyloids and Kinetic Studies of WT-TTR$_{105-115}$

Introduction to Amyloids

Amyloid proteins are insoluble fibrous protein aggregates. Accumulation of amyloid in organs can lead to amyloidosis and causes diseases such as Alzheimer's disease and type II diabetes. [1-2] At least 25 clinical disorders are associated with amyloid protein aggregation. [3] A table of various diseases associated with amyloids is shown below. [4-5]

Disease	Protein Featured
Alzheimer's disease	Beta amyloid
Type II diabetes mellitus	IAPP (Amylin)
Parkinson's disease	Alpha-synuclein
Rheumatoid Arthritis	Serum amyloid A
Dialysis related amyloidosis	β-2-Microglobulin
Atherosclerosis	Apolipoprotein AI
Huntington's disease	Huntington

Table 3-1. A list of some of the diseases associated with amyloids

Many amyloid fibrils have a common core structure; significant numbers of them are long and straight without branching and have diameters of 70-120 Å which gives a

characteristic birefringence upon binding with Congo Red dye. Numerous amyloid fibrils also display a cross-β diffraction pattern. [6]

Amyloid fibrils have been characterized by electron microscopy, [7] mass spectrometry, [8] cryo-EM reconstruction, [9] atomic force microscopy, x-ray diffraction, [10] circular dichroism, [6] and NMR spectroscopy. [11-12] The process of amyloid formation is known to involve the individual polypeptide monomer units which are held together by non-covalent interactions. The peptide monomers form β-sheets, either parallel or anti-parallel which are stabilized by the hydrogen bonding forces. [13] One or more of the β-sheets then associate into a protofilament, and the winding of the protofilaments results in assembly of the microscopic fibril. [13] Amyloid fibrils are able to be formed from small polypeptide fragments of fully denatured conformations; larger sequences comprising of 80 to 150 residues require the presence of more compact or partially folded states to form amyloids. [14]

It is important to understand the mechanism of amyloid fibril formation. To understand this mechanism, the structure of the fibrils, the unfolded protein and its native state must be determined. The structural information from fibrils and proteins may provide indications of the mechanism of amyloid fibril formation, which could subsequently lead to more effective treatment and prevention of various diseases. [6, 15-17]

A protein fragment of interest is transthyretin$_{105\text{-}115}$ ($TTR_{105\text{-}115}$). This protein fragment forms amyloid fibrils at pH =2.0 and has the sequence YTIAALLSPYS. [7] It has been studied extensively in R.G. Griffin's laboratory [18] and is a suitable model

system because many of its interstrand distances have been reported. WT-$TTR_{105-115}$ contains a stack of β-sheets, which consist of in register, parallel peptide fibers. The interstrand distances, determined experimentally, within a β-sheet vary between 4.41 Å and 4.59 Å. The stacked sheets are anti-parallel, -1 residue out of register. AFM measurements of the protofilaments heights have shown that each protofilament consists of four sheets. However, recent STEM data indicates that there are two sheets per protofibril, consistent with MAS NMR spectra.

$TTR_{105-115}$ is a serum protein, which is synthesized primarily in the liver, as well as the choroid plexus and retina. $TTR_{105-115}$ can form amyloid fibrils, which are then deposited in extracellular regions, causing neuro-degeneration and organ failure. The treatment of $TTR_{105-115}$ amyloid diseases is currently limited to liver transplantation. [18-20]

WT-$TTR_{105-115}$ is a model system that can be used to conduct initial MAS NMR-DNP experiments as described in chapter 5. Developed DNP methods on WT-$TTR_{105-115}$ can then be used on larger systems, such as PI3-SH3.

Kinetic Studies of WT-$TTR_{105-115}$ and L111M-$TTR_{105-115}$

The kinetics of fibril formation can be assessed by monitoring optical turbidity, binding of amyloid fibrils to a fluorescent dye such a thioflavin T, dynamic light scattering, time-resolved circular dichroism, or NMR [6, 21]. In all cases, kinetic measurements in a wide variety of systems show that fibril formation is preceded by a characteristic lag or nucleation phase, followed by a period of rapid growth and then fibril maturation.

Solution NMR can be used to study fibril formation kinetics because the completely formed amyloid fibril precipitates as a solid and does not contribute to the NMR spectra in solution; the disappearance of signal intensity can be used to monitor fibril growth. Kinetic studies using solution NMR were conducted by dissolving the WT-$TTR_{105-115}$ (obtained from CS Bio) at 15 mg/mL concentration in 10% deuterated acetonitrile at pH =2.0 .The kinetics of fibril formation was monitored by ^{1}H solution NMR at 591 MHz. The pulse sequence used incorporated presaturation for water suppression, allowing the peptide signal to be observed. Experiments were conducted at 37°C. Each experiment was repeated several times. Figure 3-1 below shows two of the kinetics studies for the WT-$TTR_{105-115}$ as well as a 1D spectrum of WT-$TTR_{105-115}$. Note that the lag time for WT-$TTR_{105-115}$ seems to vary. This difference in lag phase is most likely associated with the amount of impurities present in the sample that may act as a seeding mechanism. The initial phase is called the lag or nucleation phase of fibril formation. The next phase is the rapid fibril growth phase which is similar for both curves. The final phase is the fibril maturation phase. Further studies can be conducted to study the kinetics of L111M and compare these kinetic results with those of WT-$TTR_{105-115}$. Also, further studies can be conducted to investigate the effect of impurities on fibril growth kinetics.

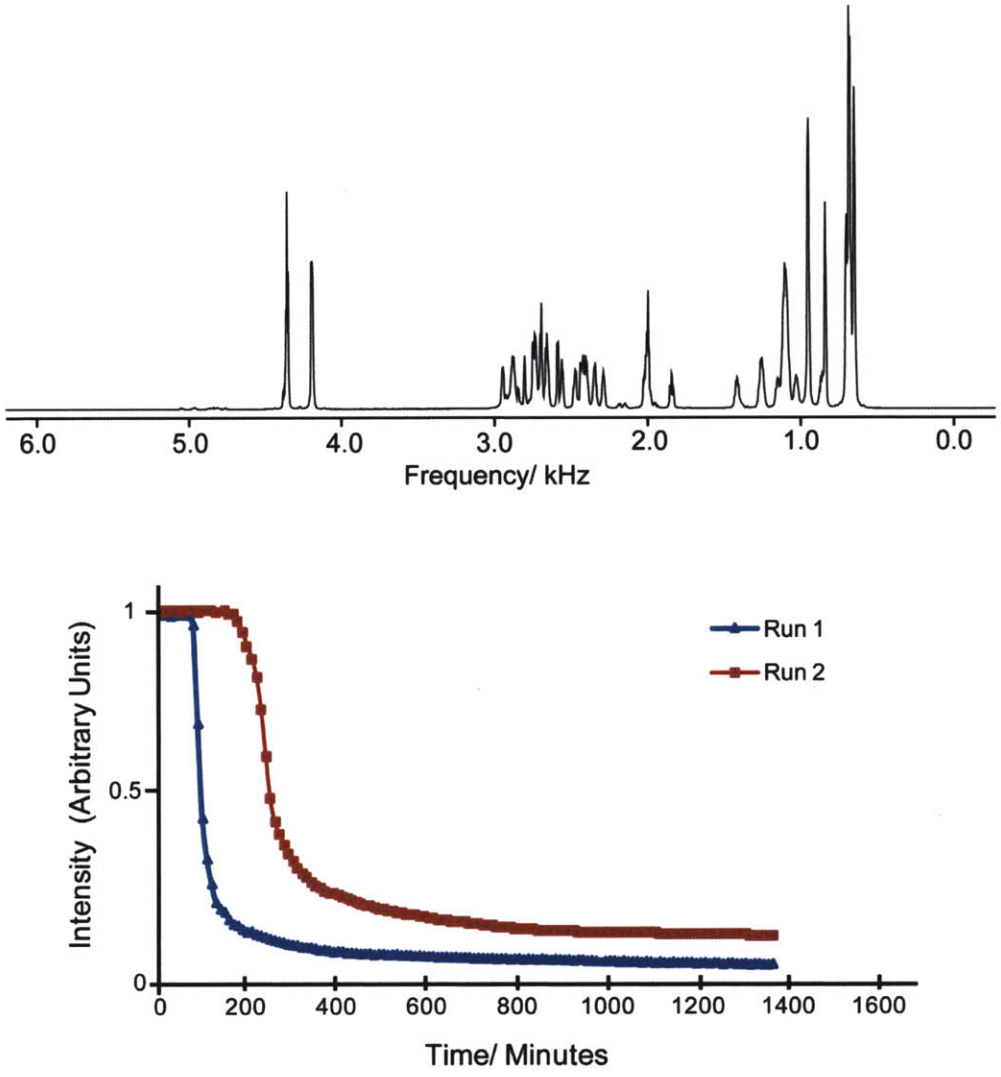

Figure 3-1. a) 1D ^{1}H spectrum of WT-TTR$_{105\text{-}115}$ fibrils with solvent suppression before fibril growth b) the kinetics of amyloid fibril formation in WT-TTR$_{105\text{-}115}$ monitored by solution state NMR. Although the lag phase is different, which is most likely due to seeding, the kinetics are the same.

References

1. Tycko, R., Characterization of amyloid structures at the molecular level by solid state nuclear magnetic resonance spectroscopy. *Amyloid, Prions, and Other Protein Aggregates, Pt C* **2006,** *413*, 103-122.
2. Petkova, A.; Ishii, Y.; Balbach, J. J.; Antzutkin, O. N.; Leapman, R. D.; Delaglio, F.; Tycko, R., A Structural Model for Alzheimer's b-Amyloid Fibrils Based on Experimental Constraints from Solid State NMR. **2002**.
3. Sunde, M. B., C.C.F., From the globular to the fibrous strate: protein structure and structural conversion in amyloid formation. . *Q. Rev. Biophys.* **1998,** *31* (1), 39.
4. Teplow, D. B., Preparation of amyloid beta-protein for structural and functional studies. *Amyloid, Prions, and Other Protein Aggregates, Pt C* **2006,** *413*, 20-33.
5. Tycko, R., Progress towards a molecular-level structural understanding of amyloid fibrils. *Curr. Opin. Struct. Biol.* **2004,** *14* (1), 96-103.
6. Guijarro, J. I.; Sunde, M.; Jones, J. A.; Campbell, I. D.; Dobson, C. M., Amyloid Fibril Formation by an SH3 Domain. *Proc. Natl. Acad. Sci. U. S. A.* **1998,** *95*, 4224-4228.
7. Serpell, L. S., M.; Fraser, P.E.; Luther, P.K.; Morris, E.P.; Sangren, O.; Lundgren, E.; Blake, C.C.F., Examination of the Structure of the Transthyretin Amyloid Fibril by Image-Reconstruction from Electron-Micrographs. *Journal of Molecular Biology* **1995,** *254* (2), 6.
8. Nettleton, E. J. T., P.; Sunde, M.; Bouchard, M.; Dobson, C.M.; Robinson, C.V., Characterization of the oligomeric states of insulin in self-assembly and amyloid fibril formation by mass spectrometry. *Biophysical Journal* **2000,** *79* (2), 12.
9. Jimenez, J. L.; Guijarro, J. I.; Orlova, E.; Zurdo, J.; Dobson, C. M.; Sundae, M.; Saibil, H. R., Cryo-electron Microscopy Structure of an SH3 Amyloid Fibril and Model of the Molecular Packing. *EMBO J.* **1999,** *18* (4), 815-821.
10. Diaz-Avalos, R.; Long, C.; Fontano, E.; Balbirnie, M.; Grothe, R.; Eisenberg, D.; Caspar, D. L., Cross-beta order and diversity in nanocrystals of an amyloid-forming peptide. *J Mol Biol* **2003,** *330* (5), 1165-75.
11. Tycko, R., Solid-state NMR as a probe of amyloid fibril structure. *Curr. Opin. Chem. Biol.* **2000,** *4* (5), 500-506.
12. Petkova, A. T.; Ishii, Y.; Balbach, J. J.; Antzutkin, O. N.; Leapman, R. D.; Delaglio, F.; Tycko, R., Structural Model for Alzheimer's beta-Amyloid Fibrils Based on Experimental Constraints from Solid State NMR. *Proc. Nat'l Acad Sci* **2002,** *99*, 16742-16747.
13. Ghahghaei, A. F., Nasim, Review: structure of amyloid fibril in diseases. *J. Biomedical Science and Engineering* **2009,** *2*, 13.
14. Hall, D. H., Nami; Dobson, Christopher M., A Toy Model for Predicting the Rate of Amyloid Formation from Unfolded Protein. *Journal of MOlecular Biology* **2005,** *351* (1), 10.
15. Cottingham, M. G.; Hollinshead, M. S.; Vaux, D. J. T., Amyloid Fibril Formation by a Synthetic Peptide from a Region of Human Acetylcholinesterase that is Homologous to the Alzheimer's Amyloid-b Peptide. *Biochemistry* **2002,** *in press*.

16. Paravastu, A. K.; Petkova, A. T.; Tycko, R., Polymorphic fibril formation by residues 10-40 of the Alzheimer's beta-amyloid peptide. *Biophysical Journal* **2006,** *90* (12), 4618-4629.
17. Meier, J. J.; Kayed, R.; Lin, C. Y.; Gurlo, T.; Haataja, L.; Jayasinghe, S.; Langen, R.; Glabe, C. G.; Butler, P. C., Inhibition of human IAPP fibril formation does not prevent beta-cell death: evidence for distinct actions of oligomers and fibrils of human IAPP. *American Journal of Physiology-Endocrinology and Metabolism* **2006,** *291* (6), E1317-E1324.
18. Jaroniec, C. P., C.E. MacPhee, N.S. Astrof, C.M. Dobson, R.G. Griffin,, Molecular Conformation of a Peptide Fragment of Transthyretin in an Amyloid Fibril. *Proc. Nat'l. Acad. Sci.* **2002,** *99,* , 16748-16753.
19. Jarvis, J. A.; Craik, D. J.; Wilce, M. C. J., X-Ray DiffractionStudies of Fibrils Formed FromPeptide Fragments ofTransthyretin. *Biochemical and Biophysical Research Comm.* **1993,** *192* (3), 991-998.
20. McPhee, C. E.; Dobson, C. M., Chemical Dissection and Reassembly of AMyloid Fibrils Formed by a Peptide Fragment of Transthyretin. *J. Mol. Biol.* **2000,** *297*, 1203-1215.
21. Liu, L. M., R.M., Kinetics of inhibition of beta-amyloid aggregation by transthyretin. *Biochemistry* **2006,** *45* (51), 15702-15709.

CHAPTER 4. Distance Measurements by DNP-enhanced double-quantum filtered DRAWS experiments

Adapted from a manuscript in preparation for submission to Communication by Thorsten Maly, Rebecca Mayrhofer and Robert G. Griffin.

Francis Bitter Magnet Laboratory and Department of Chemistry Massachusetts Institute of Technology Cambridge, MA, 02139, USA,

NMR signal intensities of solids and liquids can be enhanced by several orders of magnitude with dynamic nuclear polarization (DNP). DNP, therefore, is potentially an important tool for a variety of applications, ranging from particle physics [1, 2] and pharmaceutical applications [3, 4] to structural and mechanistic studies of biologically relevant molecules [5, 6]. During a DNP experiment, microwave irradiation of the sample drives the transfer of the large thermal polarization of a paramagnetic polarizing agent to the nuclei of interest with the maximum expected enhancement given by the gyromagnetic ratios, γ_S/γ_I , of the electrons (S) and the nuclei (I) (660 for $e^-/^1H$).

The largest signal enhancements in solids at high magnetic fields (>5 T) are observed in experiments that exploit the cross-effect (CE) as the dominant DNP mechanism [7, 8]. The underlying mechanism is a three-spin process that is operative when the nuclear Larmor frequency (ω_{0I}) is smaller than the inhomogeneous breadth, Δ, of the EPR spectrum of the paramagnetic polarizing agent. The cross effect involves two electrons with Larmor frequencies ω_{0S1} and ω_{0S2} and the enhancement is

maximized when the difference between the electron Larmor frequencies approximates the nuclear Larmor frequency ($|\omega_{0S1} - \omega_{0S2}| \approx \omega_{0I}$, matching condition).

In recent years, solid-state NMR (ssMR) has become an important technique to determine structures of biological macromolecules. The technique relies on high precision measurements of distances and torsion angles, thus allowing the determination of high-resolution structures, comparable to those obtained by x-ray crystallography. SSNMR techniques are especially important for macroscopically disordered or complex systems, such as membrane proteins or amyloid fibrils [7-9], whose structures are not accessible by x-ray crystallography.

However, many SSNMR experiments to measure distances or torsion angles are based on the excitation and reconversion of double-quantum coherences, which are notoriously inefficient to excite and detect, and therefore requiring extensive signal averaging [9]. For example, the double-quantum efficiency in a double-quantum filtered version of DRAWS (dipolar recoupling with a windowless sequence, DQF-DRAWS) is typically of the order of 20-30 %. The situation is further aggravated by the intrinsic low sensitivity of SSNMR for large biological molecules due to their size and limited sample amount in the rotor. Therefore, the overall low sensitivity of SSNMR techniques dictates the necessity to combine these methods with DNP for signal enhancement and to acceleration of acquisition times.

In this communication, we demonstrate that the DQF-DRAWS experiment can be significantly accelerated when combined with DNP. From the experimental data the ^{13}C-^{13}C-distance in a model compound is determined by numerical simulation and the

results are compared with measurements performed on crystalline material without DNP. Both experiments yield similar results and no influence of the paramagnetic polarizing agent and the low temperature was found.

Results and Discussion

Figure 4-1 (top trace) shows the DNP-enhanced ^{13}C-CPMAS spectrum of a frozen solution of 500 mM 1,3-^{13}C-^{13}C malonic acid and 10 mM TOTAPOL in d_6-DMSO/D_2O/H_2O. A single line at 175.4 ppm is observed, because only the two carbon atoms of the carbonyl groups are isotopically labeled. At a temperature of 90 K and a microwave power of 2.5 W (estimated at the position of the sample), an enhancement of $\varepsilon > 120$ is observed. This is slightly lower than the factor of $\varepsilon \sim 180$ typically measured for a solution of 2 M ^{13}C-Urea and 10 mM TOTAPOL in d_6-DMSO/D_2O/H_2O under similar conditions [10]. The lower enhancement, which is the ratio of signal intensities recorded with and without DNP (off-signal), can be attributed to the following two factors. First, it was difficult to acquire an off-signal with sufficient signal-to-noise ratio because of the dilute sample that was used to suppress any intermolecular dipolar interactions, which would compromise distance measurements. Second, the signal from the malonic acid overlapped with the signal from trace amounts of ^{13}C contained in the stator material (Figure 4-1, asterisk). The signal arising from the impurity further complicated estimation of signal enhancement due to DNP, but had no affect on the actual distance measurements.

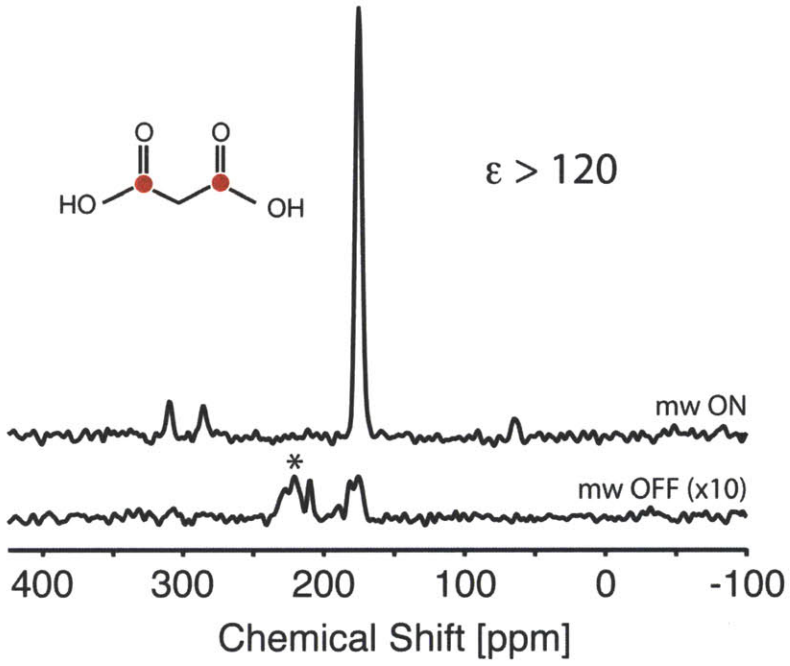

Figure 4-1. 1D ^{13}C-CPMAS NMR spectrum of a frozen solution of 500m M 1,3-$^{13}C_2$ malonic acid (labeling positions are given in the inset) and 10 mM TOTAPOL in d_6-DMSO/D_2O/H_2O. Top trace: spectrum recorded with DNP. Bottom trace: spectrum recorded without DNP (off signal). The asterisk indicates stator impurities. Experimental parameters: $\omega_r/2\pi$ = 5.882 kHz, T = 90 K, 4 scans are averaged, microwave polarization time 30 s.

The steady-state bulk-polarization in the DNP experiment is reached after 30 s of microwave irradiation and a build-up constant τ_B of 5 s was determined (data not shown). Based on this result, the polarization time was set to 6.25 s (1.25* τ_B) to achieve the maximum enhancement per unit time.

Double-quantum build-up curves for 1,3-^{13}C-^{13}C malonic acid measured with and without DNP are presented in Figure 4-2 and both experiments yield identical results. Using numerical simulations, a distance of 2.85 Å was determined, which is in good agreement with previously reported distances of 2.56 to 2.67 Å determined by SSNMR [9, 11, 12]. To accurately fit the experimental data points, a Gaussian distribution of distances was assumed and the optimum value for σ was found to be σ = 0.25 Å.

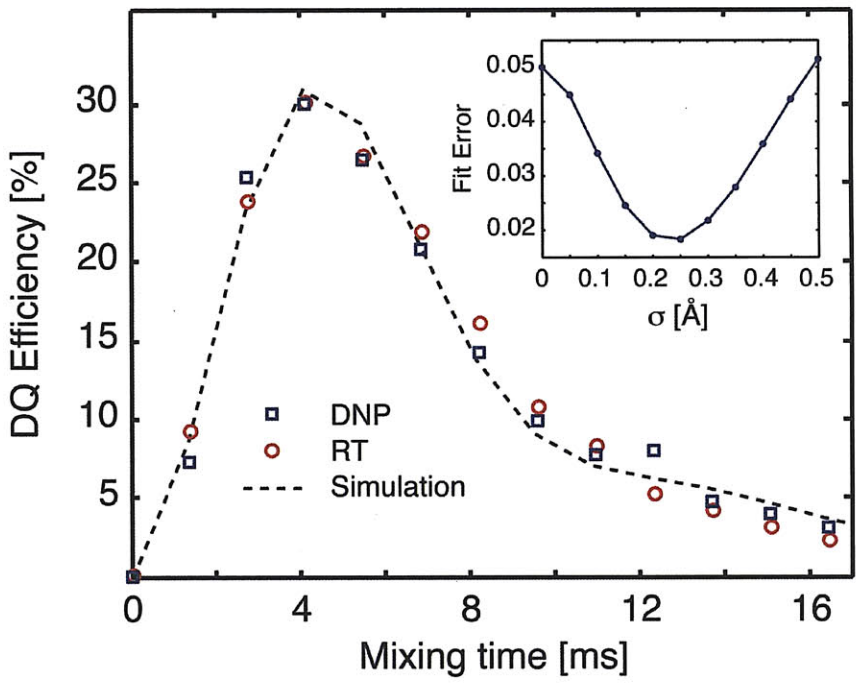

Figure 4-2. DQF-DRAWS curve of 1,3-$^{13}C_2$ malonic acid with and without DNP and numerical simulation. The inset shows the fitting error for different values of σ. Experiment parameters: $\omega r/2\pi$ = 5.882 kHz, 100 kHz ^{1}H decoupling, 50 kHz ^{13}C power, T = 90 K, microwave polarization time 6.25 s, 16 scans (for DNP). For room temperature measurements 80 transients were average and the recovery delay was set to 60 s.

With the large signal enhancements available through DNP, it is possible to accelerate dramatically the otherwise very time-consuming DQF-DRAWS measurements. Here, the total acquisition time for DNP-enhanced DQF-DRAWS experiments was < 30 minutes, while more than 20 hours of signal averaging was necessary in the case of the crystalline material. In parts, the long averaging times for the crystalline material are due to the fact that malonic acid has a longer ^{1}H T_1 than the ammonium salt that is typically studied [13]. However, approximately factor 30 more sample material had to be used for measurements on the crystalline sample. Therefore the overall gain of the DNP experiment over measurements on the crystalline material is still factor > 120.

The emphasis of this study is on DNP-enhanced DQF-DRAWS experiments that are performed in frozen glassy solutions at low temperatures (< 90 K). Therefore, the sample material was not re-crystallized to obtain a single conformation, which would be necessary for measurements of the crystalline material. However, glassy frozen solutions can induce different conformations of a small molecule as already seen in pulsed EPR measurements performed on tyrosine molecules in a glycerol/water mixture [14]. Since the malonic acid molecule is not planar [15] it is most likely that the observed distance distribution is a result of the glassy environment. This is not the case for larger molecules or bio-macromolecules and no distance distributions are expected for such systems.

In this short communication we presented DNP-enhanced DQQ-DRAWS measurements performed on a model system. We showed that DNP-enhanced experiments yield identical results compared to measurements performed at room temperature even in the presence of 10 mM TOTAPOL, the paramagnetic polarizing agent.

Experimental

1,3-^{13}C-^{13}C - Malonic acid (99 %) was purchased from Cambridge Isotopes (Andover MA, USA) and used without further re-crystallization. For DNP experiments, the material was dissolved in a mixture of d_6-DMSO/D_2O/H_2O (60/34/6, w/w/w) with a final concentration of 500 mM. The sample also contained 10 mM TOTAPOL as the polarizing agent [10] and was packed in a 2.5 mm sapphire rotor (~6 µl). For room-temperature experiments 1,3-^{13}C-^{13}C - Malonic acid was packed in a 2.5 mm zirconia rotor.

DNP experiments were performed on a custom-designed 211 MHz DNP/NMR spectrometer, using a 2.5 mm triple-resonance (e^-, ^1H, ^{13}C), cryogenic MAS probe equipped with a commercial stator (Revolution NMR, Inc.). The spectrometer operates at a magnetic field of 5 T, corresponding to an electron Larmor frequency of 140 GHz. High-power microwave radiation (> 10 W) was generated by a gyrotron, a vacuum-electronic device, operating at a frequency of 139.662 GHz [16-18]. Cryogenic temperatures were achieved by spinning with cold drive and bearing gas [19, 20]. Room-temperature experiments were performed on the same instrument.

Numerical simulations of the dq-DRAWS experiment were performed using SpinEvolution simulation software [21].

References

1. Goertz, S.T., The dynamic nuclear polarization process. Nucl. Instrum. Methods Phys. Res., Sect. A, 2004. 526(1-2): p. 28-42.
2. Wind, R.A., et al., Applications of dynamic nuclear polarization in 13C NMR in solids. Prog. NMR. Spec., 1985. 17: p. 33-67.
3. Gallagher, F.A., et al., Magnetic resonance imaging of pH in vivo using hyperpolarized 13C-labelled bicarbonate. Nature, 2008. 453(7197): p. 940-943.
4. Day, I.J., et al., Investigation of the Potential of the Dissolution Dynamic Nuclear Polarization Method for General Sensitivity Enhancement in Small-Molecule NMR Spectroscopy. Appl. Magn. Reson., 2008. 34(3): p. 453-460.
5. Maly, T., et al., Dynamic nuclear polarization at high magnetic fields. J. Chem. Phys., 2008. 128(5): p. 052211-19.
6. Barnes, A.B., et al., High-Field Dynamic Nuclear Polarization for Solid and Solution Biological NMR. Appl. Magn. Reson., 2008. 34(3): p. 237-263.
7. Hu, K., et al., Dynamic nuclear polarization with biradicals. J. Am. Chem. Soc., 2004. 126(35): p. 10844-5.
8. Farrar, C.T., et al., Mechanism of dynamic nuclear polarization in high magnetic fields. J. Chem. Phys., 2001. 114(11): p. 4922-4933.
9. Karlsson, T., et al., A Study of Homonuclear Dipolar Recoupling Pulse Sequences in Solid-State Nuclear Magnetic Resonance. J. Am. Chem. Soc., 2003. 125(24): p. 7394-7407.
10. Song, C., et al., TOTAPOL: a biradical polarizing agent for dynamic nuclear polarization experiments in aqueous media. J. Am. Chem. Soc., 2006. 128(35): p. 11385-90.
11. Gregory, D.M., et al., Windowless dipolar recoupling: the detection of weak dipolar couplings between spin 1/2 nuclei with large chemical shift anisotropies. Chem. Phys. Lett., 1995. 246(6): p. 654-663.
12. Gregory, D.M., et al., Determination of local structure in solid nucleic acids using double quantum nuclear magnetic resonance spectroscopy. J. Chem. Phys., 1997. 107(1): p. 28-42.
13. Chang, J.J., R.G. Griffin, and A. Pines, Carbon-13 chemical shielding tensors in ammonium hydrogen malonate. J. Chem. Phys., 1975. 62(12): p. 4923-4926.
14. Warncke, K., G.T. Babcock, and J. McCracken, Static Conformational Distributions in the Solid State: Analysis and Application to Angular Dispersion in Side Chain Orientations in Model Tyrosine in Aqueous Glass. J. Phys. Chem., 1996. 100(11): p. 4654-4661.
15. Jagannathan, N.R., S.S. Rajan, and E. Subramanian, Refinement of the crystal structure of malonic acid, C3H4O4. J. Chem. Cryst., 1994. 24(1): p. 75-78.
16. Becerra, L., et al., Dynamic nuclear polarization with a cyclotron resonance maser at 5 T. Phys. Rev. Lett., 1993. 71(21): p. 3561-3564.
17. Granatstein, V.L., R.K. Parker, and C.M. Armstrong, Vacuum electronics at the dawn of the twenty-first century. Proc. IEEE, 1999. 87(5): p. 702-716.
18. Joye, C., et al., Operational Characteristics of a 14-W 140-GHz Gyrotron for Dynamic Nuclear Polarization. IEEE Transactions on Plasma Science, 2006. 34(3): p. 518-523.

19. Allen, P.J., et al., Apparatus for low-temperature magic-angle spinning NMR. J. Magn. Reson., 1991. 92(3): p. 614-617.
20. Barnes, A., et al., Cryogenic sampe exchange NMR probe for magic angle spinning dynamic nuclear polarization. J. Magn. Reson., 2009. 198: p. 261-270.
21. Veshtort, M. and R. Griffin, SPINEVOLUTION: a powerful tool for the simulation of solid and liquid state NMR experiments. J. Magn. Reson., 2006. 178(2): p. 248-82.

CHAPTER 5. Probe Construction and Testing for MAS NMR-DNP

Performing solid state NMR experiments with concurrent high frequency microwave irradiation at cryogenic temperatures requires several new pieces of instrumentation in addition to the traditional ones. In solid state NMR experiments, the sample is contained in a probe allowing mechanical spinning at the "magic angle" of the sample rotor as well as application of strong B_1 fields at the nuclear Larmor frequency. Spinning at the "magic angle" averages anisotropic interactions that otherwise would lead to broad spectral linewidths and low resolution and sensitivity. Microwaves generated by a gyrotron are delivered to the probe via a corrugated waveguide (see Figure 2-3). [1] The sample rotor is spun with cooled nitrogen gas, which brings the probe top to a temperature of 80 K. Cooling of the nitrogen gas is achieved by passing the gas through a pressurized heat exchanger can, allowing for continual filling and operation. A custom made sample eject system allows for sample changes at cryogenic temperatures without disturbing the probe. [2].

MAS NMR DNP experiments on a 2.5 mm probe were conducted on Ala-108 ^{13}CO WT-TTR$_{105\text{-}115}$ fibrils to determine the enhancement and the performance of the probe for DNP experiments on a small fibril system. Enhancements of 80-100 were achieved with 15 mM TOTAPOL in a mixture of 60%/32%/8% d_8 glycerol/D_2O/H_2O (v/v/v). The Figure below shows a spectrum of Ala-108 ^{13}CO WT-TTR$_{105\text{-}115}$ fibrils with and without DNP. This cross polarization spectrum was taken at 90 K at a MAS frequency of 4.5 kHz.

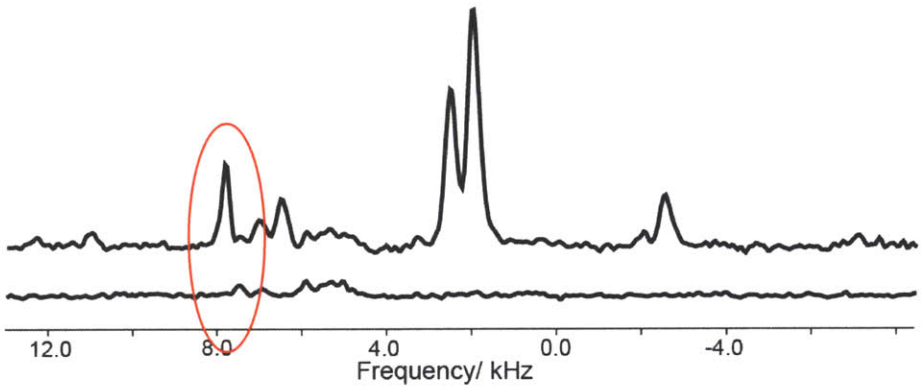

Figure 5-1. DNP on Ala-108 ^{13}CO WT-$TTR_{105-115}$fibrils. The off spectrum (bottom spectrum) does not contain a carbonyl peak, circled in red, whereas the on spectrum (top spectrum) does. The glycerol in the sample also gets enhanced as shown. The enhancement achieved with 15 mM TOTAPOL in a mixture of 60/32/8 d_8 glycerol/D_2O/H_2O (v/v/v) is 80-100.

As can be seen by the absent signal in the off spectrum, the signal to noise ratio is too low to detect any peaks without DNP. This is because the 2.5 mm probe has a very small sample volume (6 µL) resulting in poor signal to noise ratio. A larger sample volume, such as that of a 4 mm rotor, would improve the signal to noise ratio, providing a better off-signal and allowing for less efficient experiments such as DQDRAWS (see chapter 1). Thus, a partially constructed 4 mm probe was finished for the purpose of conducting a wide range of MAS NMR DNP experiments with a good signal to noise ratio (less data acquisition time).

Parts Construction

Sample Eject

A sample eject system, which saves valuable time between sample changes, was designed, following closely the design produced by Alexander Barnes for the 380 MHz spectrometer. [2] The sample eject system consists of a sample eject pipe, a funnel and a tube which guides the rotor out of the spectrometer and into a receiving box. Therefore, it is not necessary to disturb the probe during sample changes and a new sample can be inserted within a few minutes. Figure 5-2 below shows a photograph of the sample eject, funnel and transfer tube.

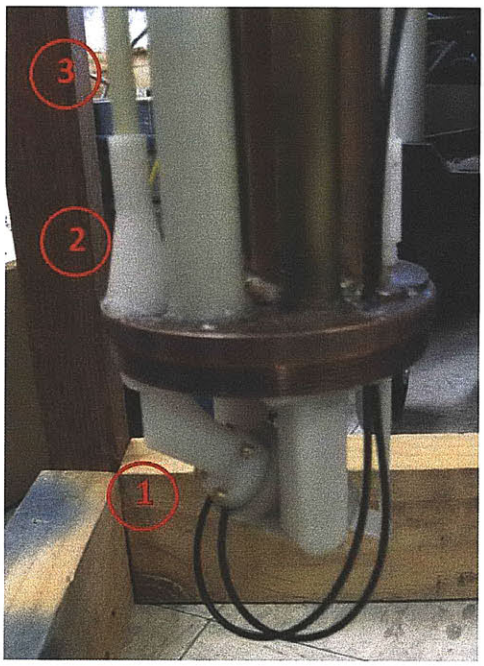

Figure 5-2. Photograph of the sample eject system. During sample eject, the rotor is forced out of 1) the stator into the 2) sample eject, through the 3) funnel, the 4) transfer tube and finally out of the probe into a receiving box.

The sample eject pipe and the funnel were designed in Autodesk Inventor™ and were made by AGS, Inc. using 3D printing. Both of these pieces are made of acrylonitrile butadiene styrene (ABS), the same material used for electronic equipment cases such as computer monitors and keyboards. It is a common thermoplastic used to make light, rigid, molded products. This material combines both the strength and rigidity of the acrylonitrile and styrene polymers with the toughness of the polybutadiene rubber even at low temperatures. As the sample eject must work at temperatures ranging from 75 Kelvin to 298 K, this material is ideal. The tube that leads the rotor out of the spectrometer is made of G-10 plastic, also resistant to low temperatures. This material was chosen because it is readily available. The sample eject pipe, funnel and transfer tube make up the sample eject system designed for the 4 mm probe.

In Solid State NMR probes, the sample spins at a magic angle. The sample is spun by providing both drive and bearing pressures which allows the sample to be spun at fast MAS frequencies. The drive and bearing gas is room temperature nitrogen gas for room temperature experiments and cooled nitrogen gas for cryogenic experiments. The sample eject is driven by the room temperature nitrogen gas – the rotor ejects through the dewar into a transfer tube which then leads the sample out of the magnet and into a receiving box. Before the receiving box, the rotor's speed is slowed by passing through some Teflon tubing which prevents damage of the rotor. During ejection, the rotor must be turned from an angle of 54.7^{o} (the magic angle) with respect to the magnetic field to 0^{o} with respect to the magnetic field to exit the magnet. The sample eject design allows for the rotor to make this turn smoothly during exit and entry. The funnel on top of the sample eject allows for magic angle adjustments. [2]

During the sample exchange process, the spinning is stopped and the bearing and drive gas valves are closed. A high pressure burst of room temperature nitrogen gas is injected into the exhaust pipe which enters the sample chamber, forcing the rotor out of the stator, into the sample eject pipe, through the funnel, into the transfer tube and finally into the receiving box. The eject pipe is sealed with GORE-TEX to ensure that the nitrogen gas flows out of the stator, through the sample eject pipe, funnel and transfer tube.

To insert the rotor into the stator, a small flow of room temperature nitrogen gas enters the exhaust pipe to help ease the rotor into the stator, preventing damage of the rotor. Although room temperature gas is used for the sample exchange process during cryogenic temperature operation, it does not raise the temperature of the sample cavity significantly. This is because the heat capacity of the sample cavity is large enough that the temperature does not increase significantly. The whole sample exchange process and bringing the probe back to its desired temperature takes no more than 10 minutes.

Exhaust Pipe

The exhaust pipe was designed using Autodesk Inventor™ and was built by Jeffrey Bryant of the Griffin Lab. The Figure below shows the Autodesk drawing of the exhaust pipe.

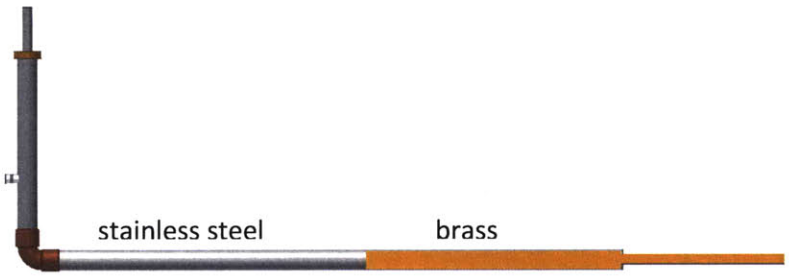

Figure 5-3. Autodesk drawing of the vacuum jacketed exhaust pipe for the 4 mm 211 MHz probe. The exhaust pipe is made of stainless steel and brass as indicated. The end of the exhaust pipe is not vacuum jacketed to allow the lower part of the probe to cool down efficiently without cooling the entire probe which would result in a cooling power loss.

As shown in the Figure, the vacuum jacketed exhaust pipe consists of stainless steel and brass. The conductivity of stainless steel is 16 W/m K and the conductivity of brass is 100 W/ m K. This allows the lower part of the probe, where the sample is located, to cool down efficiently. The decreased conductivity of the stainless steel prevents the upper part of the probe from cooling down too much which would result in frost buildup and cooling power loss. Note that the bottom of the exhaust pipe is not vacuum jacketed. This assists in cooling the lower part of the probe quickly and efficiently, allowing the probe to reach a desirable temperature of ~80 Kelvin.

Magic Angle Adjust Changes

In previous designs, the magic angle could not be adjusted at cryogenic temperatures. This is because the delrin plastic threads bind to the copper threads in the copper base plate, making it impossible to adjust the magic angle. As the plastic shrinks during the cool down process, the magic angle is shifted slightly. Accordingly, the section of the plastic MAS adjust piece which runs through the copper base plate

was replaced with brass and also larger threads following the preliminary tests done by Evgeny Markhasin. Cold temperature tests conducted with the 4 mm 211 MHz probe has shown that binding at cryogenic temperatures is dramatically decreased, allowing the magic angle to be adjusted at these low temperatures. The Figure below shows a spectrum of KBr after magic angle adjustments at cold temperature. Prior to adjusting the magic angle, the KBr rotational echoes went out to approximately 6 ms. After adjusting the magic angle, the rotational echoes extended beyond 10 ms, a vast improvement.

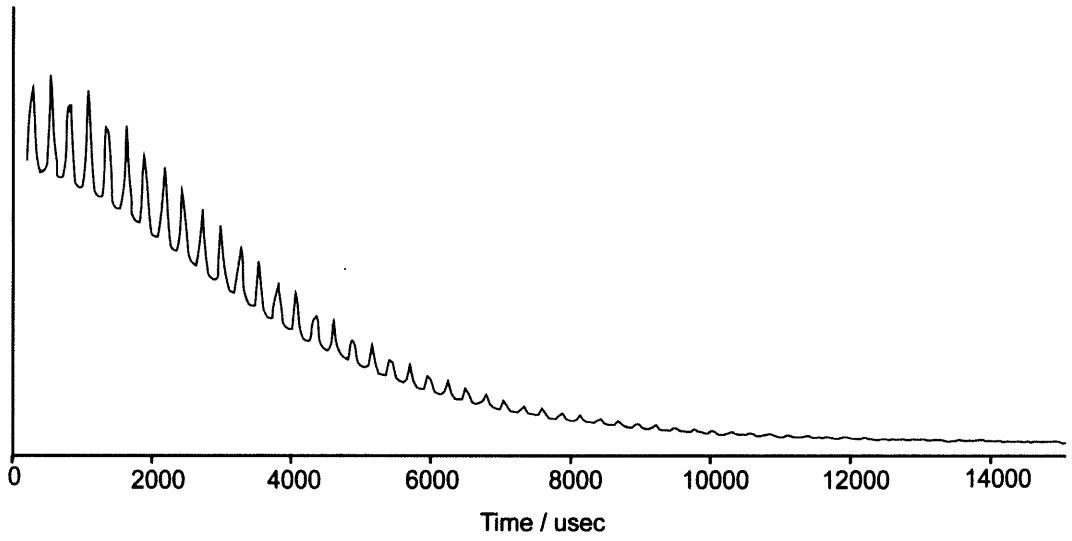

Figure 5-4. Rotational echoes of KBr after adjusting the magic angle at 83 K. Prior to adjustment, the rotational echoes extended to 6ms; after adjustment, the rotational echoes extended beyond 10ms. Sample was spun at a MAS frequency of 3.7 kHz MAS, the recycle delay was 1 second and 32 scans were acquired.

Room Temperature Experiments

Upon completion of the remaining parts of the probe as well as modifications to the probe, room temperature experiments were conducted to determine the

performance of the probe. After successfully tuning and calibrating the probe powers, shimming was conducted using 1-^{13}C glycine. The Figure below shows a 1-^{13}C- glycine spectrum before and after shimming. The linewidth before shimming was 200 Hz and after shimming, 25 Hz.

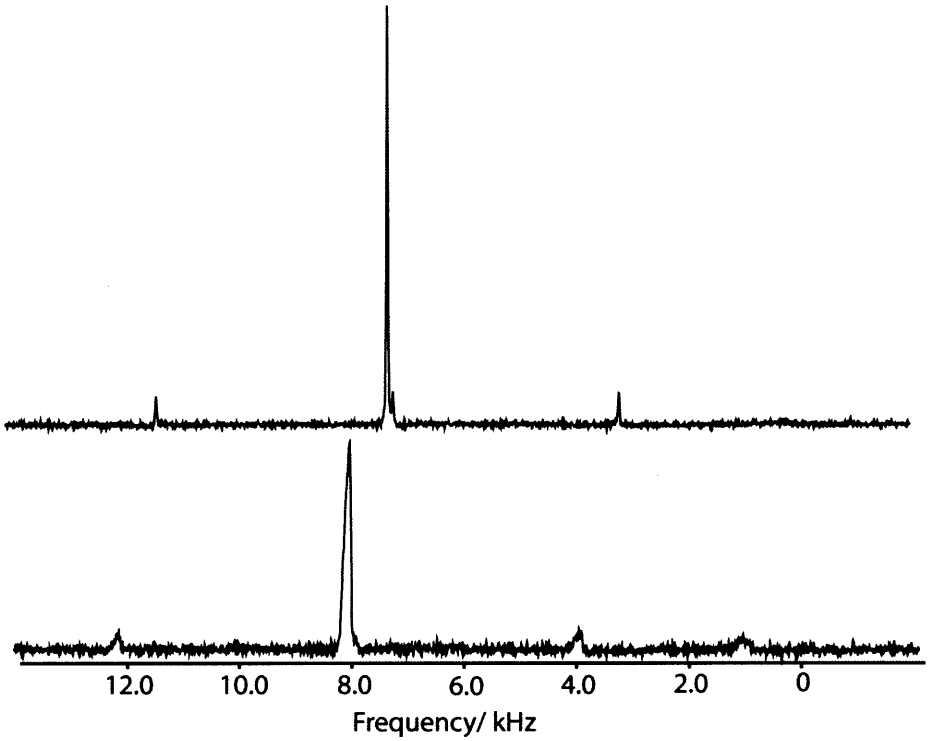

Figure 5-5. 1D ^{13}C spectrum of 10% 1-^{13}C glycine before shimming (bottom spectrum) and after shimming (top spectrum). The sample was spun at a MAS frequency of 4.125 kHz. The linewidth decreased from 200 Hz to 25 Hz.

Cold Temperature Tests

After completion of room temperature tests, the performance of the probe was tested at cryogenic temperatures. The final temperature achieved after cooling was 83 K. After tuning, adjusting the magic angle, and calibrating the powers at cryogenic temperatures, DNP on U-^{13}C, ^{15}N urea was conducted. The Figure below shows the

signal enhancement obtained at various microwave powers. The maximum signal enhancement achieved is 160 which can be seen in the power dependence curve.

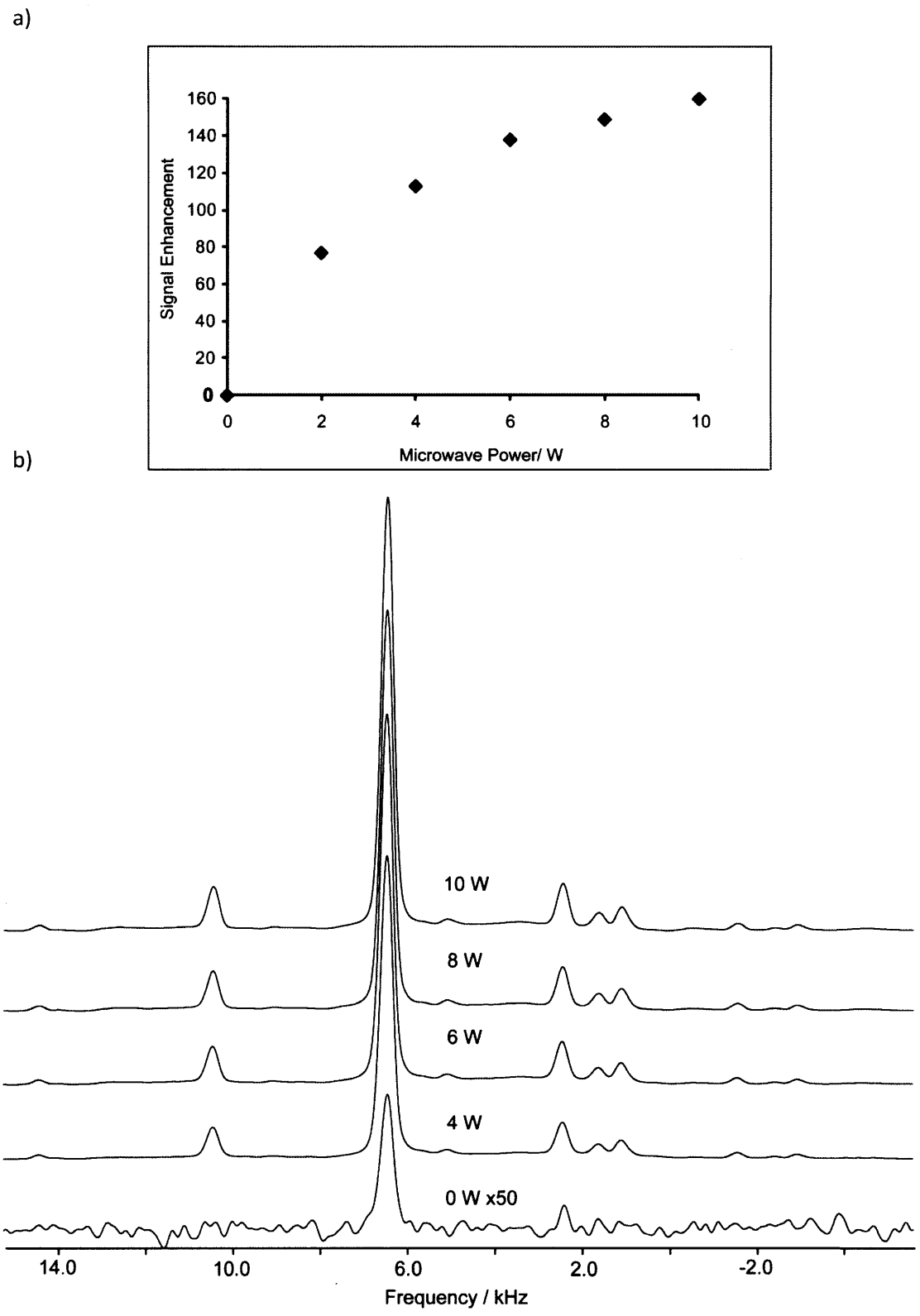

Figure 5-6. a) Microwave power dependence curve b) 1D ^{13}C CP-DNP spectra of U-^{13}C, ^{15}N Urea at 4W, 6W, 8W, and 10W microwave power. The off signal is included and scaled by a factor of 50. The sample was spun at a MAS frequency of 4.125 kHz at a temperature of 85 K.

Future Experiments

The partially built 4 mm 211 MHz probe was completed and its performance was tested at room temperature and cryogenic temperatures. The maximum DNP enhancement obtained is 160. The 4 mm 211 MHz probe can be used to further investigate MAS NMR-DNP on amyloids such as WT-$TTR_{105-115}$. This probe is a powerful tool for obtaining high signal to noise ratio spectra in a short time and can be utilized for fast elucidation of structural information of proteins and fibrils.

References

1. Barnes, A. B.; Paëpe, G. D.; Wel, P. C. A. v. d.; Hu, K.-N.; Joo, C.-G.; Bajaj, V. S.; Mak-Jurkauskas, M. L.; Sirigiri, J. R.; Herzfeld, J.; Temkin, R. J.; Griffin, R. G., High Field Dynamic Nuclear Polarization for Solid and Solution Biological NMR. *Applied Magnetic Resonance* 2008, (in press).
2. Barnes, A. B.; Mak-Jurkauskas, M. L.; Matsuki, Y.; Bajaj, V. S.; Wel, P. C. A. v. d.; DeRocher, R.; Bryant, J.; Sirigiri, J. R.; Temkin, R. J.; Lugtenburg, J.; Herzfeld, J.; Griffin, R. G., Cryogenic sample exchange NMR probe for magic angle spinning dynamic nuclear polarization. *Jour. Magnetic Resonance* 2009,

Curriculum Vitae

EDUCATION

Massachusetts Institute of Technology, Ph.D. Physical Chemistry 2007-2010
University of Illinois at Urbana-Champaign, B.S, cum laude 2003-2006

PUBLICATIONS

Franks, WT; Wylie, BJ; Schmidt, HLF, et al (2008). "Dipole tensor-based atomic-resolution structure determination of a nanocrystalline protein by solid-state NMR." Proceedings of the National Academy of Sciences of the United States of America **105** (12): 4621-4626

Heller, DA; Mayrhofer, RM; Baik, S, et al. "Concomitant length and diameter separation of single-walled carbon nanotubes." Journal of the American Chemical Society **126**(44): 14567-14573

Heller, DA; Barone, PW; Swanson, JP, et al. "Using Raman spectroscopy to elucidate the aggregation state of single-walled carbon nanotubes." Journal of Physical Chemistry, B **108**(22): 6905-6909